Thesis

Mechanical Modeling of Human Platelets Membrane

Mathieu Sayeur, cmr

Submitted in partial fulfillment of the requirements

For the Master of Applied Science in Biomedical Engineering

Department of Mechanical Engineering

Faculty of Engineering

University of Ottawa

Contents

Figures

Tables

Legend

Symbols:

L_p	Platelet aspiration length	W	Energy strain function
R_p	Pipette radius	I_1, I_2	Invariants of a 2-D tensor
R_s	Undeformed platelet major radius	$\lambda_s, \lambda_\theta$	Meridional/Equatorial stretch ratio
S_s	Undeformed platelet minor radius	T_θ, T_s	Meridional/Equatorial stretch ratio
r_θ	Principal curvature in the equatorial direction	T_0	Pre-stress (residual)
r_s	Principal curvature in the meridional direction	$T_{S\theta}$,$T_{\theta S}$	Shear stresses
r_n	Principal curvature at the normal of the meridional and equatorial intercept.	c_1, c_2, c_3	Material constants
Φ, φ	Phi, angle away from the axis of symmetry (Z)	Z, dZ	Length / differential length along the Z axis
Φ_1, φ_1	Phi, boundary angle between zone 1 and zone 2.	R_Z, r	Underformed/deformed distance away from the Z axis
Φ_3, φ_3	Phi, boundary angle between zone 2 and zone 3.	dR_Z, dr	Underformed/deformed differential distance away from the Z axis
A_o, A	Underformed/deformed platelet surface area	S,s	Underformed/deformed distance along a surface meridional
V_o, V	Underformed/deformed platelet volume	dS, ds	Underformed/deformed differential distance along a surface meridional
ε	Epsilon, numerical zero	Θ, θ	Angle coordinate along a surface equatorial plane
p_o	Atmospheric pressure	$d\Theta, d\theta$	Differential angle coordinate along a surface equatorial plane
p_i	Aspiration pressure	SR	Platelet initial shape ratio
p	Internal platelet pressure		

Acronyms:

AFM	Atomic Force Microscopy	OCS	Open Canalicular System
cAMP	Cyclic Adenosine Monophosphate	PE	Pulmonary Embolism
DTS	Dense Tubular System	ULVWF	Ultra Large VWF
DVT	Deep Vein Thrombosis	VTE	Venous Thromboembolism
MHV	Mechanical Heart Valves	VWF	Von Willebrand Factor
MVB	Multivesicular Bodies		

Abstract

In an effort to help understand the mechanical properties of human platelets, their deformations were measured using micropipette experiments over an aspiration pressure range of 1-5 cmH_2O, in steps of 1 cmH_2O. The experiments confirmed the previously reported linear relationship between deformation and pressure. The experimental results were used to determine the material constants of a thin-axisymmetric shell model based on a strain-energy constitutive relation to describe the platelet deformations under aspiration. The model was successful in capturing the experimental deformations. It also suggested that the mechanical properties of human platelets are not significantly influenced by their volumes, but do vary depending on the platelets' undeformed shape ratios. In addition, the model suggested that platelet membrane ruptures due to micropipette aspiration may be strain-related. The limitations of the experimental methods arising from direct contact with reactive cells such as platelets are highlighted, prompting the need for developing new methods which will not require the use of inhibition agents that alter the platelets' mechanical properties.

Afin d'approfondir les connaissances des propriétés mécaniques des plaquettes humaines, leurs déformations ont été mesurées lors d'expériences avec des micropipettes pour des pressions d'aspiration de 1-5 cmH_2O, par intervalles de 1 cmH_2O. Les expériences ont confirmé la relation linéaire entre les déformations et la pression d'aspiration telle que précédemment publié. Les données expérimentales ont été utilisées pour déterminer les constantes matérielles d'un modèle de membrane mince axisymétrique basé sur une loi de comportement caractérisant l'énergie de déformation. Le modèle simule bien les déformations des plaquettes sous aspiration; il suggère également que les propriétés mécaniques des plaquettes humaines ne sont pas influencées significativement leur volume, mais varient en fonction de leurs formes avant déformation. De plus, le modèle suggère que les ruptures de la membrane des plaquettes sous aspiration seraient reliées aux déformations. Les limites des méthodes expérimentales utilisées, du fait du contact direct avec des cellules aussi réactives que les plaquettes sont soulignées, et mettent l'emphase sur le besoin de mettre au point de nouvelles méthodes ne requérant pas d'agents d'inhibitions qui altèrent les propriétés mécaniques des plaquettes.

Acknowledgements

First, I would like to thank my supervisor, Dr. Michel Labrosse, for his patience and understanding, as well for his support and guidance. I would also like to extend my gratitude to Dr. Antonio Giulivi of the Ottawa General Hospital for his generous supply of human platelets, as well as to Dr. Geoff Mealing and his staff at the NRC for their support and for allowing me to use their facilities and equipment to conduct my experiments.

Second, I want to thank the Canadian Forces for offering me the possibility to continue my education with their financial contribution; I am especially thankful to my supervisors who have provided me with the flexibility I required in my work schedule.

Last, but surely not least, I would like to thank my wife and life partner for believing in me, for supporting me through the storms, and for finally letting me see the sun shine through dark clouds.

Thank you.

1 Introduction

In the United States alone, there is an average 274 people who die from blood-clot related health issues every day (National Blood Clot Alliance). The most prevalent diseases associated with blood clotting are deep vein thrombosis (DVT) and pulmonary embolism (PE), together referred to as venous thromboembolism (VTE). There are approximately 100 in 100,000 persons each year who will have a first instance of VTE, with six percent recurrence after 6 months. Six percent of DVT and twelve percent of PE cases lead to mortality within 1 month (R. H. White, 2003). In the United States, this problem is receiving more and more attention due to its morbidity, mortality and cost: the average yearly cost per cases of DVT and PE are $10,804 and $16,664 respectively (Spyropoulos & Lin, 2007), totaling more than $1.5 billion per year (Dobesh, 2009).

The main risks factors for VTE are age, immobilisation, underlying diseases or conditions (cancer or pregnancy for example), major surgery and trauma. For example, between 30% to 50% knee and hip surgery patients will have a VTE related event, and the incidence rate is as high as 50 to 60% for patients with head trauma or leg fractures (Buller, 2009). Other risks factors include genetic predispositions such as deficiencies in antithrombin, protein C, or protein S, and drugs use such as oral contraceptives and hormonal replacement therapies (Buller, 2009). Risks factors generally lead to thrombosis by one of the following three mechanisms, known as the Virchow's triad: blood flow stasis, hypercoagulability or endothelial injury (Golan & Tashjian, 2012).

All these mechanisms have in common the fact that they can activate an essential component of the clotting process, namely, a cell called the blood platelet. This cell has been extensively studied from biological and pharmacological points of view; however, very little of its mechanical properties is known to this day. This lack of knowledge is a significant concern in cases such has mechanical heart valves (MHV) implantations which require patients to be administered anticoagulant treatments for the remainder of their lives (Wei Yin, Bluestein, Jestyz, & Perrotta, 2002). Such treatments put patients at increased risk of

prolonged bleedings, and thus significantly reduce their quality of life, and involve significant health care costs. This has prompted the need for better designed MHVs which would not induce platelet activation (Edmunds et al., 1997).

In parallel to this effort, this thesis aims at contributing to increase knowledge of the mechanical properties of human platelets, using a constitutive model defined and characterized by experimental observations. It builds on previous efforts, notably on the validation of the model soundness, carried out by McGrath et al., 2011, on mouse platelets, which enabled the continuation of the experimentations to proceed to human platelets. Dr. Michel Labrosse formulated the model geometric mathematical definition, its constitutive equations and its MatLab code implementation. After a thorough review of these previous contributions, I carried out experimental measurements on human platelets using the micropipette aspiration technique and confirmed the applicability of the model to human platelets. Then, I used the model to predict the mechanical response of human platelets under specific loads, and to assess the influence of model parameters on the material constants obtained and overall simulated platelet behavior.

2 Literature Review

2.1 Platelets Description

Platelets are the smallest cells in the human circulatory system, with diameters ranging between 2-5 µm, thicknesses of approximately 0.5 µm, and volumes of 6-10 fL (Michelson, 2006). They are very active in homeostasis (internal regulation and stability) of the circulatory system by detecting and rectifying damages to its membranes, and are extremely reactive to their environment. They also provide necessary support to the blood coagulation process (Levin, 2013). They are subcellular fragments of megakaryocytes found in the blood, and are non-nucleated cells which live on average for 7 days (Hartwig, 2013). In short, they are complex systems, with specialized functions involving numerous mechanical and chemical processes. This section will outline the structure and functions of platelets, to provide an understanding of the significant contributors to their mechanical properties.

2.1.1 Platelet Structure

In order to properly understand the mechanical properties of the platelets, it is important to qualify their various structures along with their properties and interactions. The following paragraphs will present the platelets external and internal structures, as well as their associated organelles.

The platelet, in its normal state while in blood flow, looks like it has a rugged surface composed of small recessions and bumps, as can be seen in Figure 1. The platelet surface is not continuous; small openings form interconnected serpentine tunnels, which are called the open canalicular system (OCS). The platelet membrane system consists of a thick exterior plasma membrane, called glycocalyx, covering the traditional lipid bi-layer membrane found in most cells, the OCS, a dense tubular system (DTS), Golgi complexes, and a sub-membrane composed of thin filaments playing a role in its shape transformation and its receptors translocation. The glycocalyx is a very active component of the platelet; it

serves as a sensor for changes in its environment requiring platelets response, and it does so via its embedded glycoproteins. The most populous receptors on the glycocalyx are the (GP) Ib-IX-V and the integrin $\alpha_{IIb}\beta_3$ (also known as the GPIIb-IIIa complex), with an approximate average count of 25,000 and 80,000 respectively. Both these receptors are mobile and linked to the submembrane cytoskeleton. Any increase in the surface of the lipid bi-layer is hypothesized to come from the OCS and membrane folds (J. G. White, 2013). The surface increase can reach as much as 420% of the resting platelet surface. The DTS is a separate system from the OCS, dispersed within the platelet cytoplasm, but it forms a close grid-like relation with it, a fenestrated membrane system, where their respective membranes are almost juxtaposed.

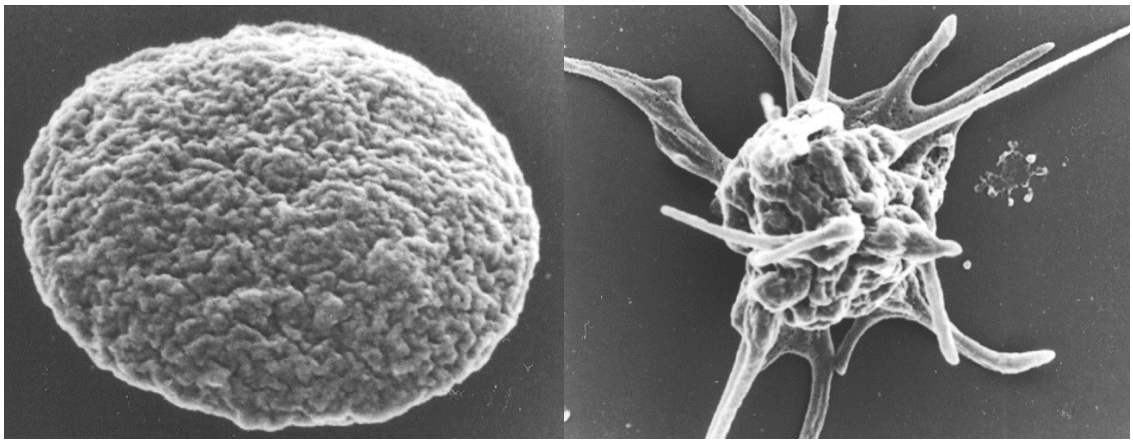

Figure 1. Platelet photographed using a low-voltage, high-resolution scanning electron microscope (LVHR-SEM), left is in its suspension discoid shape, and right is in its activated state with dendritic extension. Reproduced with permission (J. G. White, 2013).

The platelet intracellular matrix is a liquid gel materiel with a significant amount of fibrous components, including a dense microtubule coil around its circumference, and an actomyosin filament system. Finally, the matrix also contains glycogen and vesicles. The microtubule coil is a single tubule of approximately 25 nm in diameter wound around the platelet between 3-24 times, and is presented in Figure 2. It acts as the platelet cytoskeletal

support system, and gives it its discoid form in the inactivated state (J. G. White, 2013). The actomyosin filament system is composed of roughly half the actin molecules present in the rested platelet, and it is partially linked to the submembrane cytoskeleton, while the remainder anchors organelles across the intracellular matrix. During platelet activation, the actomyosin filament system constricts and pulls the microtubule coil and the organelles together to form a dense center in the platelet, from which pseudopods extend (J. G. White, 2013).

Figure 2. Fixed platelet cross section where the microtubule coil around its equatorial circumference is indicated by the black arrow. Reproduced with permission (J. G. White, 2013).

Platelets contain three principal organelles, the α granules, dense bodies (also named δ granules) and lysosomes. Other important organelles present in the platelet are mitochondria, glycosomes, electron dense chains and clusters, and tubular inclusions (J. G. White, 2013). Platelets also sometimes present multivesicular bodies (MVB). For the scope

of this thesis, only the α granules are worth describing in further detail, but it is important to note the non-homogeneity of the platelets' cytoplasm. The α granules are normally separated from each other in healthy platelets; they are 200-500 nm in diameter and contain Von Willebrand Factors (VWF) and various proteins. The α granules have greater density at their centers than at their peripheries. They are the most numerous organelles in platelets (J. G. White, 2013).

2.1.2 Platelet Functions

Platelets are systems primarily designed to detect abnormal environmental conditions (i.e. tissue damage) and react quickly to initiate healing and maintain homeostasis. They are able to do so under high fluid shear stresses while in the blood circulatory system. While several complex chemical processes enable platelets to achieve their mission, they will not be discussed in great detail as they are outside the scope of this thesis. Instead, the main functionality of the platelets will be discussed in simple terms, along with its structural or mechanical relevance.

First, platelets need to be close to the walls of blood vessels to be able to detect an injury on their linings. The platelets' discoid shapes and small sizes allow them to be pushed away from the center of the blood vessels; the platelets keep their shapes due to a long microtubule wrapped around itself multiple times. Various glycoproteins on the platelets' surface can either bind to their environment or detect chemicals within their vicinity. This makes the platelets able to detect changes in their environment such as tissue damage, and/or to detect other platelets activity. The glycoprotein receptors are also capable of moving along the platelet membrane, thanks to the reorganisation the actin filaments in the submembrane. Glycoprotein mobility serves as a shock absorber for the platelets trying to adhere to an injury site in the circulatory system, effectively slowing the platelets down and allowing for more binding sites. Once bonded to the site of injury, platelets need to cover as much area as they can to form a hemostatic plug. This is enabled again by glycoprotein mobility, but also by the actin filaments reorganisation within the cytoplasm, and the extra membrane surface area generated by the unfolding of the OCS. However, one

platelet cannot completely cover the injury by itself and it needs to communicate and collaborate with other platelets to form an effective plug. They do so by storing significant amounts of “message” chemicals in their granules, and releasing them upon detection of the injury site. Platelets agglomerate together, using their long pseudopods as extended arms, to form a blood clot. Once the injury has healed, a platelet needs to remove itself from the site of injury, and does so by contracting its cytoskeleton and breaking free from its bonds.

2.2 A word of caution about experiments on platelets

As with most research areas in biomedical engineering, a significant challenge in studying platelets resides in the variance between in-vitro experimental data and the in-vivo reality. For instance, the degree of fidelity of an in-vitro experiment is hard to evaluate, because the in-vivo environment parameters vary according to age, ethnicity, health, and so on. As will be described below, many factors affect platelets characteristics when performing in-vitro research and render experimental results somewhat difficult to translate to the in-vivo context.

2.2.1 Use of Platelets Inhibitors and Their Effects on Platelets

Without the use of anti-coagulants, blood would start clotting upon collection. Platelets being meant to react to changes in their environment, they would not be able to be studied in their inactivated state without the use of inhibiting agents as blood samples are collected and platelet-rich plasma is prepared. This however, has an effect on platelets, depending on the type of anti-coagulant used. Discussed below are various substances commonly used along with their effects on platelets functions.

2.2.1.1 Citrate

One of the most well-known effects of citrate anti-coagulant is to increase the platelets aggregations induced by ADP (Gibbins & Mahaut-Smith, 2004). This process

happens via two different mechanisms; the enhanced one involves the creation of thromboxane by ADP, which does not normally occur at physiological divalent cations concentrations. Thromboxane is a potent platelet activation agent as it initiates intracellular release of ionized calcium. However, citrate also has the effect of significantly reducing the ionic concentration of calcium in the plasma, by an order of magnitude (Gibbins & Mahaut-Smith, 2004; Hayward & Moffat, 2013). Reduced ionic calcium in the plasma impairs the proper functioning of the integrin $\alpha_{IIb}\beta_3$ receptors (Phillips et al., 1997), essentially defeating the predominant chemical and mechanical receptor of platelets.

2.2.1.2 Theophylline and Adenosine

To reduce the agonist effect of citrate on ADP-induced platelet activation, theophylline can be used in concentrations ranging between 1-4 mM. It inhibits ADP activation by increasing the synthesis of cyclic adenosine monophosphate (cAMP), which in turn reduces cytoplasmic levels of ionized calcium (Burns & Dodge, 1984). Since calcium is required for actin reorganisation within the platelets cytoskeleton, theophylline effectively reduces the platelets' ability to change their shapes (Hartwig, 2013). When used in conjunction with prostaglandin E_1, it inhibits the formation of thromboxane, prostaglandin E_2 and $F_2\alpha$, in activated platelets, further preventing the increase in intracellular calcium levels (Burns & Dodge, 1984). Adenosine also increases the synthesis of cAMP, and has similar effects as Theophylline (Haslam & Lynham, 1972).

2.2.1.3 Other activation inhibitors

Other common activation inhibitors, such as heparin and ethylenediaminetetraacetic acid (EDTA) were not considered herein, as being outside the practice of previously established methods (McGrath, 2009).

2.3 Cellular Mechanical Testing

2.3.1 Atomic Force Microscopy

Atomic force microscopy (AFM) is generally synonymous with the indentation of a cell by a probe moving over its surface (Hochmuth, 2000), although it has recently evolved into more complex applications. In brief, using AFM, nanometer scale displacements can be measured by noting the position of a laser beam reflected off a probe tip held by a cantilever-type beam, which is connected to a piezoelectric actuator controlling the probe movements (Ethier & Ethier, 2007). A detailed description of the various cantilever configurations with their associated models and applications can be found in Song and Bhushan (2008) (Song & Bhushan, 2008). AFM can provide localized information on a cell, depending on tip geometry and size, as well as on cell stiffness, in resolution ranging from tens to hundreds of nanometers (Ethier & Ethier, 2007). The value of AFM resides in its ability to provide relatively high resolution mapping of cells or molecules in their natural environment, taking into account biological complex assembly patterns, dynamic behaviour, and interactions ability (Gaczynska & Osmulski, 2008). One drawback of this method, however, is that it cannot detect forces under 10-15 pN due to molecular collisions (thermal) interference (Hochmuth, 2000). This method has been used in a variety of different ways, to image elastic properties of platelets and bacteria, to image proteins and DNA, to measure the binding forces between single molecules, and to determine the elastic properties of bone, bone marrow and gelatin (Radmacher, Fritz, Kacher, Cleveland, & Hansma, 1996).

Recent AFM research in the platelets field has focused on determining molecular level interactions. Among others, the study of the platelet integrin receptor GPIIb-IIIa and fibrinogen interaction, which plays a critical role in platelets adhesion on biomaterial surfaces and subsequent thrombogenesis, has led to the suggestion that binding of the integrin receptor is independent of the material surface properties once the receptor-binding epitope is exposed (Agnihotri, Soman, & Siedlecki, 2009). Also, this study reported

the debonding range for this binding complex to be in the 50-80 pN range at loading rates of 10-60 nN/s. Another study demonstrated that platelets adhesion to and activation by titanium nitrides, a US Food and Drugs Administration approved biomaterial well regarded for its numerous qualities, was increased by the use of a stoichiometric and smoother version of the material (Karagkiozaki, Logothetidis, Kalfagiannis, Lousinian, & Giannoglou, 2009). Furthermore, Young's moduli for different platelets parts have been reported as 46.5 kPa·s for a pseudopodic projection, 29.7 kPa·s for the peripheral lamelipodium, and 6.2 kPa·s for the pseudonucleus (Lee & Marchant, 2000).

2.3.2 Optical Trapping

Optical trapping, also called optical tweezers, use the radiation pressure created by focused laser beams to measure forces in the 1-200 pN range (Ethier & Ethier, 2007). Radiation pressure is the result of photons colliding onto a surface, which changes their momentum, resulting in a net force over the subject area. An object, usually some form of micron sized beads, can be either pushed (reflection) or pulled (refraction) by a beam of photons. The reflection/refraction ratio requires close attention to ensure the net resultant force creates an effective trap. Williams (2002) presented mathematical relations to create effective optical traps, as well as single molecule applications of optical tweezers (Williams, 2002). In most optical tweezers, the forces acting on the beads are directly proportional to the distance between the focus of the photons beams and the bead center. Trap "stiffness" can therefore be quantified by measuring the position of a bead in a trap, and calibrated, so that external forces can be measured from the bead's (or beams) displacement (Williams, 2002). The target cell or molecule is "tied" to the beads by using specific coatings to create binding forces. Common applications of optical trapping include the study of molecular motors, the physics of colloids and mesoscopic systems, the mechanical properties of polymers and biopolymers (Neuman & Block, 2004). More recent applications of this technique include the study of cell membranes mechanical properties, of binding force measurement between various cell structures, and of nanoparticles manipulations (Guo & Li, 2013).

Optical trapping has proven useful to study platelets bonding mechanism and forces. In one example, the thermodynamics and kinetic of platelets integrin $\alpha_{IIb}\beta_3$ bond with fibrinogen was studied using optical-trap-based electronic force clamp, which highlighted the existence of two slip bound states with different mechanical stability over a range of 5-50 pN force (Litvinov et al., 2011). Another study focused on the von Willebrand factor (VWF), and ultra large VWF (ULVWF), A1-domain bonds with the platelets (GP) Ib-IX-V complex. It identified the unbinding force for this bond to be in increments of 6.5 pN (ristocetin induced bond) and 8.8 pN (botrocetin induced bond) for the VWF, depending on the numbers of bonds formed. In contrast, the unbinding force for the ULVWF was found to be in increments of 11.4 pN (Arya, Anvari et al., 2002). The GPIb-IX-V complex sub-unit GPIbα first leucine-rich repeat role in VWF bonding was demonstrated as contributing to the bonding strength while the second leucine rich repeat proved to be essential for the bonding to occur (Arya, López et al., 2002).

A variant of the optical trapping which does not require any physical handling of the cell has been developed. This technique is called optical stretching, and consists in shining two lasers on diametrically opposed portions of a cell, without being focused on the cell. The physics behind this technique relies on the scattering and refraction forces created at the entry and exit point of the lasers, where the scattering forces of the opposed lasers cancel each other at the center of the object, while the entry and exit forces of each laser add up on each entry and exit surfaces, creating shear forces up to 1 nN (Van Vliet, Suresh, Van Vliet, & Bao, 2003). The benefits of this technique are reduced physical interaction with the cell and reduced radiation damage (due to the unfocused beams). The technique however is limited by the following constraints: the studied cell needs to have a greater refractive index than its surrounding; the cell needs to be homogenous across its structure, and not be affected by the laser. This technique has been used on red blood cell and neutrophils, and has demonstrated strains of up to 160% (Van Vliet et al., 2003).

2.3.3 Micropipette Aspiration

In the absence of AFM and optical trapping equipment in our laboratory, the micropipette aspiration technique offered the widest range of potential mechanical force, varying between 0.01 - 1000nN (Ethier & Ethier, 2007). Micropipettes are formed by stretching fine glass tubes in a velocity, force, and heat controlled environment. They are then used, with a pressure control system, to deform the cells by partially aspirating them. Using imaging tools, the aspirated lengths and cells general geometry can be determined, along with the pipettes internal radius, which allows for the evaluation of the force-deformation relationship. This technique has been used on various cells, most notably neutrophils, erythrocytes, and outer hair cells (Ethier & Ethier, 2007), to determine elastic and viscous material properties.

Micropipette aspiration can readily help identify the solid or liquid behaviour of cells. Cells which behave like liquids will completely enter the micropipette once the aspirated length is greater than the pipette radius, while cells which behave like solids will not (Hochmuth, 2000). Viscous material properties can be determined by applying step changes in pressure and noting the time required to reach equilibrium, as well as noting the time required for the aspirated portion to shrink back to 50% of its maximum (final) value upon releasing the entire pressure (Haga, Beaudoin, White, & Strony, 1998).

2.4 Cellular Mechanical Modeling

Cells are generally modeled under one of two main categories, either following a micro/nanostructure approach or a continuum mechanics approach (Lim, Zhou, & Quek, 2006). The micro/nanostructure approach is mostly used to describe the cytoskeletal mechanics of adherent cells; however it has also been used to model some suspended cells such as red blood cells undergoing large deformations, with the intent to understand the mechanical properties of their spectrin network and membrane. The continuum approach is essentially an empirical approach to describe cells mechanics by using constitutive material

models with parameters derived from experimental data. This approach is useful to obtain detailed stress-strains distributions at the entire cell level, but it is not capable of providing molecular details as the micro/nanostructure does. The following discussion will focus on the continuum mechanics approach, with particular attention to the cortical shell-liquid core and solid viscoelastic models, before going into detailed constitutive modeling for biological membranes.

2.4.1 Cortical Shell-Liquid Core Models

There are four mainstream cortical shell-liquid core models: the Newtonian liquid drop model, the compound Newtonian liquid drop model, the shear thinning liquid drop model and the Maxwell liquid drop model (Lim et al., 2006). These variants will be described below.

It has been proposed that cells which are spherical while in suspension may be modeled as a system consisting of an external envelope wrapped around a liquid, which has can be referred to as the Newtonian liquid drop model. In a model proposed by Yeung and Evans (Yeung & Evans, 1989), the envelope is defined as an anisotropic viscous cortical shell consisting of a superficial plasma membrane covering a layer of gel. The plasma membrane is presented as the limiting factor to deformation, while the underlying gel is the main contributor the viscous properties during deformation. The cell interior is assumed to be a uniform Newtonian liquid, although potentially large bodies such as the nucleus could be altering the mechanical response of the system. The authors introduced the term “apparent” viscosity to describe the core liquid-organelle viscous response to deformation. This model has been used to study blood granulocytes flow inside micropipettes, and has demonstrated a minimum pressure threshold required to initiate deformation which was explained by membrane pre-stress (E. Evans & Yeung, 1989a). This model has limitations, however, such as the fact that it cannot model the rapid initial deformation of cells entering a micropipette (Lim et al., 2006).

The Maxwell liquid drop models have been proposed to cover the small deformations or rapid deformations scenarios. Instead of using only a viscous liquid as is the case in the Newtonian model, the Maxwell liquid is modeled as a spring and dashpot in series. This model only works for small deformations, as it was demonstrated that both the elastic and viscous constants increase with larger deformation (Dong et al., 1991; Dong and Skalak, 1992, as cited in Lim et al., 2006).

The compound Newtonian liquid drop model has been proposed to compensate for the oversimplification of the cell interior as a homogenous liquid. It has been shown that the apparent viscosity measured using a Newtonian liquid drop model continuously varies with the degree of deformation (Dong et al., 1991; Dong et Skalak, 1992; Hochmuth et al., 1993a, as cited in Lim et al., 2006). This is mostly due to the nucleus occupying a significant portion of the cell interior (21% in human neutrophils for example) while being many times stiffer and viscous than its surrounding cytoplasm (Dong et al., 1991; Guitak et al., 2000; Caille et al., 2002, as cited in Lim et al., 2006). These discrepancies with the Newtonian liquid model could be modeled as either a three-layer system or two intermixed liquids (Lim et al., 2006). The three-layer system would consist of a thin cortical shell, a thick layer of low viscosity Newtonian (or Maxwell) liquid, with a core of high viscosity Newtonian (or Maxwell) liquid. Large deformations involving the core would see higher apparent viscosity, while smaller deformations would only involve the low viscosity layer and have smaller apparent viscosity. The alternate model would consist of a mixed low and high viscosity Newtonian (or Maxwell) liquids, which would involve osmotic stresses when the liquids are separated. Small deformations would see the flow of the least viscous liquid out of the viscous one, creating osmotic pressure, while large deformations would involve both liquids.

Finally, the shear thinning liquid drop model has been proposed to explain the relationship between the apparent viscosity and the shear rate during large deformations. Essentially, this model is a Newtonian liquid model which incorporates a power-law constitutive relation between apparent viscosity and aspiration pressure (i.e. mean shear rate). This type of model best fits experimental results when compared to a pure

Newtonian liquid drop model, but still fails to account for the rapid initial deformations (Lim et al., 2006).

Recently, zebrafish embryos were studied undergoing small to large localized deformations using a micropipette injection technique. Four different injection probes (radii of 2.5, 10, 20, and 30 μm) were advanced at constant velocity into the surface of the embryos, while mapping the distance-force relationship. The study concluded that the injection force followed a power-law with order of 1.5, indicating a homogenous solid response to deformation under small strains, while the rupture force linear correlation to injector radius indicated a cortical shell-liquid core response under large strains (Liu, Wu, & Chen, 2014). This denotes the complexity of modeling requirements, which should account for deformations ranges.

2.4.2 Solid Models

Solid models have been used to describe cases where cells would achieve equilibrium after loading, and would remain deformed after loading. In general, solid models assume cells are a single homogenous viscoelastic, or elastic, material. The elastic model is a simplification of the viscoelastic one, where it is assumed that time can be neglected within the specified experimental conditions. The elastic model is not usually adequate to characterize cells mechanics, but can be used as a foundation to solve viscoelastic models using the correspondence principle (Fung, 1965, as cited in Lim et al., 2006).

2.4.3 Biological Membranes Constitutive Models

Constitutive models are meant to describe gross behavior of materials in response to mechanical loads under a specific set of conditions; it is therefore not reasonable to assume that a single constitutive relation will be able to predict materiel behaviour under all conditions (Humphrey, 2002). Water for example, follows very distinct constitutive relations depending on its phase, be it gaseous, liquid or solid. As such, it is important to follow a rigorous process when establishing constitutive relations, to ensure all conditions are

accounted for and well described. A detailed approach to constitutive modelling is presented by Humphrey (Humphrey, 2002), which is summarized by the following 5 steps (DEICE): Delineate general characteristics of the material, Establish an appropriate theoretical framework, Identify a specific functional form of the relation, Calculate values of the material parameters, and finally, Evaluate the predictive capability of the final relation. With this background definition in mind, proposed constitutive models for the red blood cells and generic biological membranes will be explored.

Red blood cells mechanical properties have been extensively studied based on the relative simplicity of their geometry and (almost) homogenous properties when compared to other cells (Fung & Tong, 1968). A constitutive model for the red blood cells sphering phenomenon from undeformed bi-concave disc geometry has been proposed by Fung and Tong (Fung & Tong, 1968). Their model assumes a cortical shell-liquid core configuration, where the membrane is treated as a thin axisymmetric isotropic, elastic and incompressible shell. They also assume that bending stresses are negligible, and they consider the membrane as only being subject to in-plane stresses (the thin shell theory concludes that the resulting out of plane stresses are equal and opposed, cancelling each other). A surface element can therefore defined as per Figure 3, where Z is the axis of rotation, S is the length of the meridional line along the surface, θ is the angle of rotation, and Φ is the angle away from the Z axis. This notation will be conserved throughout the document where uppercase notations indicate the undeformed geometry, and θ will indicate the angular position of an equatorial curvilinear plane and S the curvilinear position along the meridional plane. Given this coordinate system, Fung and Tong (Fung & Tong, 1968) describe the membranes stresses T_S and T_θ in the deformed geometry as follows, when in osmotic equilibrium:

$$\frac{\partial}{\partial s}(rT_\theta) - T_S \cos\varphi = 0; r = r_\theta \sin\varphi$$

$$\frac{T_\theta}{r_\theta} + \frac{T_S}{r_S} = \Delta p$$

where Δp is the pressure differential across the membrane. They define strains (more specifically, stretch ratios) as follows, going from an undeformed to a deformed state:

$$\lambda_\theta = \frac{r\mathrm{d}\theta}{Rd\theta} \; ; \; \lambda_s = \frac{ds}{dS}$$

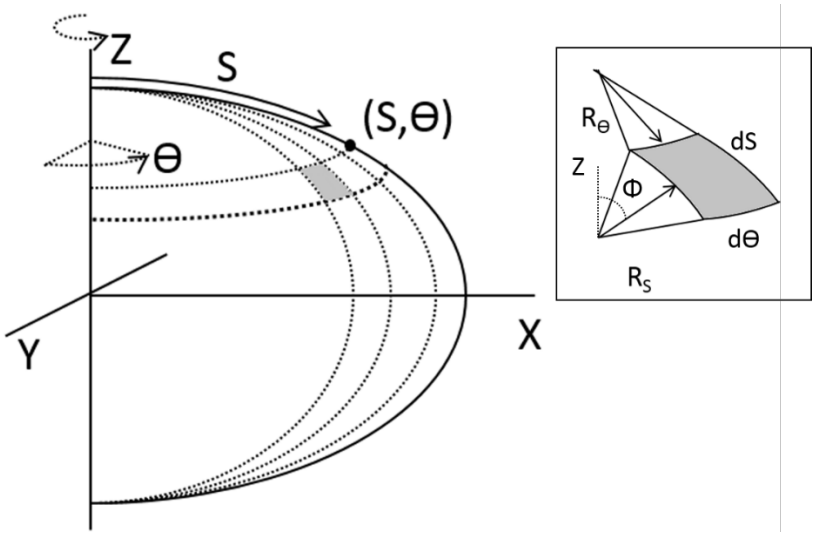

Figure 3. Curvilinear coordinate system for thin axisymmetric shell geometry.

Using these definitions, they then define the elastic properties of the red blood cell as a non-linear relation to the Young's modulus, another elastic constant, the thickness of the membrane, and the Eulerian or Lagrangian strain invariants. After further developing the geometric equations, they infer that the meridional and equatorial strains must be equal in the spherical geometry at equilibrium. They complete their model by relating the volume (constant) to define the areal change, and by constraining the geometry by using a polynomial relation between Z and X, which included three material constants. Their model did not accurately represent experimental data; however, they demonstrated that membrane deformations of red blood cells could be defined using constitutive modeling with experimental validation (McGrath, 2009).

The red blood cell model was further developed by Skalak et al (Skalak, Tozeren, Zarda, & Chien, 1973) using similar assumptions as Fung and Tong's described previously,

but using an strain energy function (W) instead of a direct elastic relationship. The proposed relation, in 2D, is as follows, where B and C are material constants:

$$W = \frac{B}{4}\left(\frac{1}{2}I_2^2 + I_1 - I_2^2\right) + \frac{C}{8}I_2^2$$

$$I_1 = \lambda_s^2 + \lambda_\theta^2 - 2\,;\; I_2 = \lambda_s^2\lambda_\theta^2 - 1$$

They provide mathematical descriptions of the stress-strains relations using the Piola-Kirchoff stress tensor, noting that the resulting relations are non-linear to either the stretch ratios or the Green material strains. Their paper reviews other forms of energy strain functions, notably one proposed for rubber known as the Mooney-Rivlin material. They also outline the following useful generalisation for any strain-energy function using two invariants:

$$T_s = 2\frac{\lambda_s}{\lambda_\theta}\left(\frac{\partial W}{\partial I_1} + \lambda_\theta^2\frac{\partial W}{\partial I_2}\right)$$

$$T_\theta = 2\frac{\lambda_\theta}{\lambda_s}\left(\frac{\partial W}{\partial I_1} + \lambda_s^2\frac{\partial W}{\partial I_2}\right)$$

Here it is interesting to note that the proposed model only allows the spherical geometry where $T_s = T_\theta$ if the energy function is a function of I_2 only, or if B = 0. Assuming no change in area would then be equivalent to assuming no membrane stresses (i.e $I_2 = 0 \;\therefore\; T_s = T_\theta = 0$) (McGrath, 2009).

Complementary to the development by Skalak et al. (Skalak et al., 1973) above, Evans (E. Evans & Yeung, 1989b) defines the red blood cell membrane tension equilibrium equations using Gaussian curvatures K_1 and K_2 as follows:

$$K_1\,T_S + K_2 T_\theta = \Delta p$$

$$\frac{\partial(r\,T_S)}{\partial s} + \frac{\partial\,T_{\theta S}}{\partial\theta}T_\theta - T_\theta\,\frac{\partial r}{\partial s} = 0$$

$$\frac{\partial(r\,T_{S\theta})}{\partial s} + \frac{\partial T_\theta}{\partial\theta}T_\theta + T_{s\theta}\,\frac{\partial r}{\partial s} = 0$$

It is interesting to note here the first equation presented is similar to the presentation of Fung and Tong (Fung & Tong, 1968), where $K_1 = \frac{1}{r_s}; K_2 = \frac{1}{r_\theta}$. Given that the Gaussian curvatures are greater than zero everywhere, then the out-of-plane stresses disappear ($T_{\theta S} = \ T_{S\theta} = 0$); also, given the homogenous material assumption (Fung & Tong, 1968), then the previous equations can be rewritten as follows:

$$T_S = \frac{1}{2K_2}\Delta p \ ; \ T_\theta = \frac{(2K_2 - K_1)}{2{K_2}^2}\Delta p$$

Or as,

$$T_S = \left(\frac{r_\theta}{2}\right)\Delta p; \ T_\theta = \left(1 - \frac{r_\theta}{2r_s}\right)\Delta p r_\theta$$

3 Methods

3.1 Platelets Deformation Model

3.1.1 Geometry and Assumptions

Non-activated platelets have been reported to be best modeled as oblate spheroids; for human platelets, a thickness over diameter ratio of 0.26 has been suggested (Frojmovic & Panjwani, 1976), while other sources have this ratio ranging between 0.10 and 0.35 (Haga et al., 1998; Michelson, 2006). In the proposed model herein, the shape ratio (S_s /R_s) has been assumed to be 0.32 to ensure continuity with a previous study in our laboratory (McGrath, 2009). In Cartesian coordinates, an oblate spheroid is essentially a sphere flattened along the Z axis, thus having a smaller meridional radius (S_s) than its equatorial radius (R_s). Figure 4 illustrates the oblate spheroidal coordinate system used for the undeformed platelet. An elemental area on the surface of this geometry is defined by its four corner points: A(R_Z, Θ, Z); B(R_Z+dR_Z, Θ, Z + dZ); C(R_Z, Θ + $d\Theta$, Z) and D(R_Z +dR_Z, Θ + $d\Theta$, Z + dZ). Φ, Θ, and S are defined as per Figure 3, and N is the normal to the (S, Θ) tangential plane. Any point on the surface is defined as follows, in uppercase notation for the undeformed geometry (McGrath, 2009).

$$X = R_s \sin\Phi \cos\Theta$$
$$Y = R_s \sin\Phi \sin\Theta$$
$$Z = S_s(1 + \cos\Phi)$$

$${R_Z}^2 = X^2 + Y^2;\ R_Z = R_s \sin\Phi$$

$$0 \le \Phi \le \pi$$
$$-\pi \le \Theta \le \pi$$

In addition, elemental variations of R_Z, Z and S on the surface are given as by

$$dR_Z = R_s \cos\Phi\, d\Phi$$
$$dZ = -S_s \sin\Phi\, d\Phi$$
$$dS = \sqrt{{dR_Z}^2 + dZ^2} = \sqrt{{R_s}^2 cos^2\Phi + {S_s}^2 sin^2\Phi}\, d\Phi$$

As for the volume and surface area of the undeformed oblate spheroid, they are, respectively

$$V_o = \frac{4}{3}\pi R_s^2 S_s$$

and

$$A_o = 2\pi R_s^2 + \pi\left(\frac{{S_s}^2}{e}\right) ln\left(\frac{1+e}{1-e}\right)$$

where:

$$e \equiv \sqrt{1 - \frac{{S_s}^2}{R_s^2}}$$

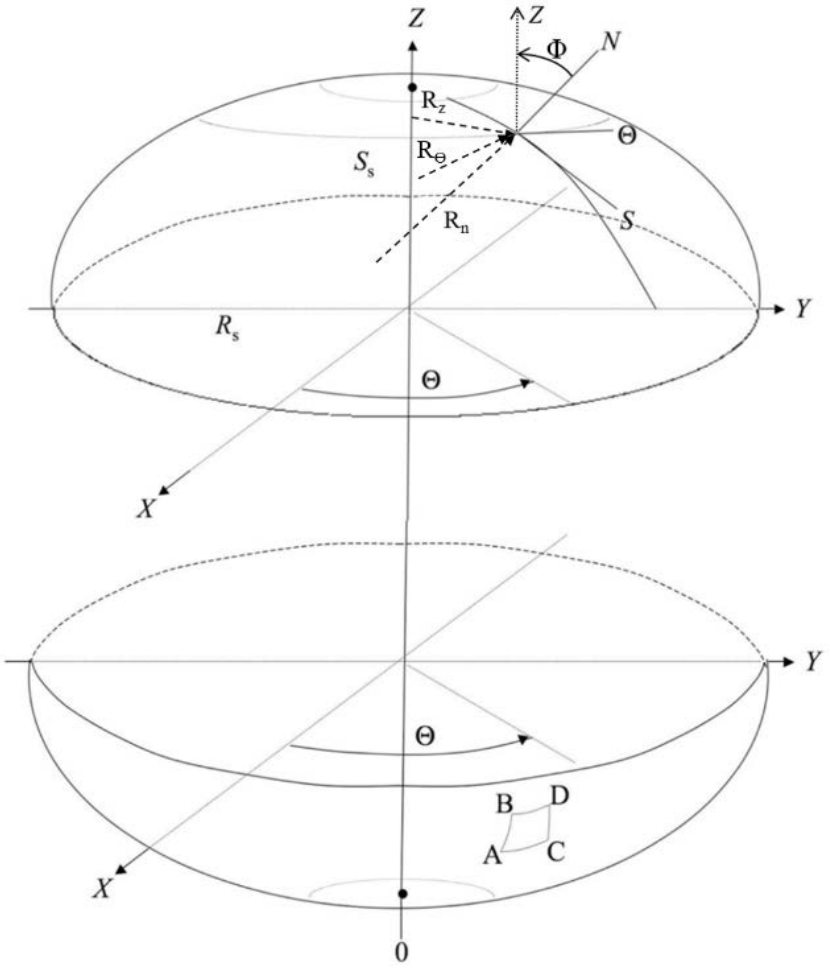

Figure 4. Oblate spheroid cylindrical and curvilinear coordinates system. Adapted from McGrath 2011 (McGrath, Mealing, & Labrosse, 2011).

Given that the platelets membrane can be modeled as a thin two-dimensional axisymmetric shell (i.e the membrane thickness is not significant to mechanical properties),

in both the undeformed and deformed states (Haga et al. 1998, as cited in McGrath, 2011), the aspirated platelet geometry can be defined as per Figure 5, where Zone 3 is the hemispherical tip of the platelet tip, Zone 2 is a cylindrical shell and Zone 1 a hemispherical shell (McGrath, 2009). For all zones:

$$r = r(z) = r_\theta \sin\varphi$$

$$\lambda_\theta = \frac{ac}{AC} = \frac{rd\theta}{Rd\Theta} = \frac{r}{R_s \sin\Phi}$$

$$\lambda_s = \frac{ab}{AB} = \frac{ds}{dS}$$

The volume and surface area of the aspirated platelet model are given, respectively, by

$$V = \frac{4}{3}\pi {r_s}^3 - \frac{\pi}{3}\left(r_s - \sqrt{{r_s}^2 - {R_p}^2}\right)^2 \left(2r_s + \sqrt{{r_s}^2 - {R_p}^2}\right) + \pi\left(L_p - R_p\right){R_p}^2 + \frac{2}{3}\pi {R_p}^3$$

and

$$A = 4\pi {r_s}^2 - 2\pi r_s\left(r_s - \sqrt{{r_s}^2 - {R_p}^2}\right) + 2\pi\left(L_p - R_p\right)R_p + 2\pi {R_p}^2 .$$

The transition point between Zone 1 and Zone 2 is described by angle φ_s between the surface normal and the Z axis. It is a constant that varies with the pipette radius (R_p), and the sphere radius r_s of Zone 1 (McGrath, 2009). Parameters λ_θ and λ_s are the membrane equatorial and meridional stretch ratios from the undeformed (ABCD) to the deformed geometry (abcd). The following expressions can be defined for Zones 1 through 3, respectively:

Zone 1:

In zone 1, the assumed spherical shape is such that the sphere radius r_s is equal to both the principal curvature radii r_n and r_θ.

$$r_\theta = r_s = r_n \; ; \; \arcsin\left(\frac{R_p}{r_s}\right) = \varphi_1 \leq \varphi \leq \pi \; ; \; \Phi_1 \leq \Phi \leq \pi$$

$$r = r_s \sin\varphi \; ; dr = ds\cos\varphi$$

$$z = r_s(1 + \cos\varphi)\,;\; dz = -ds\sin\varphi$$
$$ds = r_s\, d\varphi$$
$$\lambda_\theta = \frac{r_s \sin\varphi}{R_s sin\Phi}$$
$$\lambda_s = \left(\frac{r_s}{\sqrt{{R_s}^2 cos^2\Phi + {S_s}^2 sin^2\Phi}}\right)\frac{d\varphi}{d\Phi}$$

Zone 2:

In zone 2, the cylindrical geometry is limited by the pipette radius R_p, and therefore φ does not vary.

$$r = R_p;\; \varphi = \frac{\pi}{2}\,;\Phi_3 \le \Phi \le \Phi_1$$
$$z = r_s(1 + \cos\varphi_s) \le z \le r_s(1 + \cos\varphi_s) + L_p - R_p$$
$$dr = 0;\; dz = ds; d\varphi = 0$$
$$\lambda_\theta = \frac{R_p}{R_s sin\Phi}$$
$$\lambda_s = \left(\frac{1}{\sqrt{{R_s}^2 cos^2\Phi + {S_s}^2 sin^2\Phi}}\right)\frac{dz}{d\Phi}$$

Zone 3:

In zone 3, the hemispherical geometry is again limited by the pipette radius R_p.

$$0 \le \varphi \le \varphi_3 = \frac{\pi}{2}\,;0 \le \Phi \le \Phi_3$$
$$r = R_p \sin\varphi\,; dr = -ds\cos\varphi$$
$$z = r_s(1 + \cos\varphi_s) + L_p - R_p(1 + \cos\varphi)$$
$$d\varphi = -ds\sin\varphi$$
$$ds = R_p\, d\varphi$$
$$\lambda_\theta = \frac{R_p \sin\varphi}{R_s sin\Phi}$$
$$\lambda_s = \left(\frac{R_p}{\sqrt{{R_s}^2 cos^2\Phi + {S_s}^2 sin^2\Phi}}\right)\frac{d\varphi}{d\Phi}$$

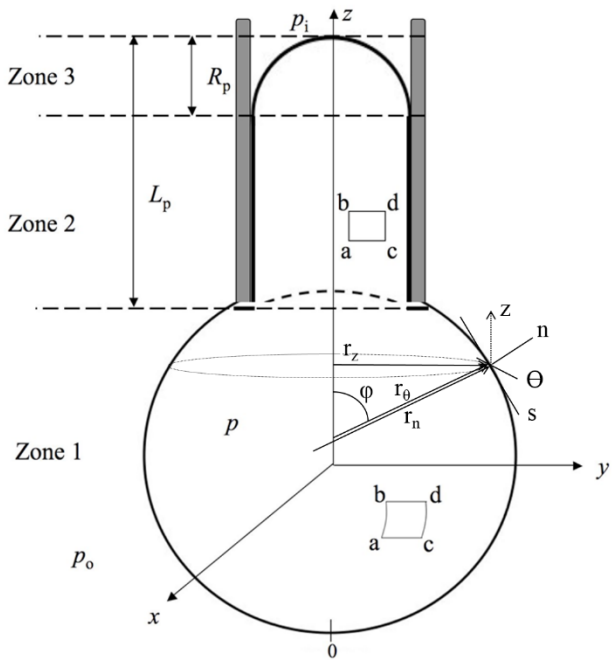

Figure 5. Aspirated platelet geometry, with coordinate systems defined as per Figure 4. Adapted from McGrath 2009 (McGrath, 2009).

3.1.2 Equilibrium and Assumptions

As mentioned previously, it is reasonable to assume that bending and radial stresses are negligible in a thin axisymmetric shell model, leaving only in-plane membrane stresses to be considered in the proposed model (E. A. Evans, 1973; Fung & Tong, 1968; McGrath, 2009; Skalak et al., 1973). Consequently, we will apply the following equations to the 3 zones of the deformed geometry, where p_i is the pressure inside the micropipette, p the intracellular pressure, and p_o the atmospheric pressure. Superscripts are added to identify zones.

$$T_S = \left(\frac{r_\theta}{2}\right)\Delta p \; ; \; T_\theta = \left(1 - \frac{r_\theta}{2r_s}\right)\Delta p r_\theta$$

$$T_S^1 = \left(\frac{r_s}{2}\right)(p - p_o) = \; T_\theta^1$$

$$T_S^3 = \left(\frac{R_p}{2}\right)(p - p_i) = \ T_\theta^3$$

Zone 2 only involves intracellular pressure as the cell membrane is constrained by the glass pipette; as such, it can be resolved by assuming that the membrane material is homogenous across all zone such as $T_S^1 = T_S^3 = T_S^2$;

$$T_S^2 = \left(\frac{r_s}{2}\right)(p - p_o) = \left(\frac{R_p}{2}\right)(p - p_i)$$

Isolating the pressure gives:

$$p = \frac{r_s p_o - R_p p_i}{r_s - R_p}$$

Finally, since the membrane is constrained by the pipette in Zone 2, then T_θ is not in relation to membrane properties and can be neglected in their characterization.

3.1.3 Constitutive Model

To be able to describe the stresses and strains relationship occurring during the platelet aspiration, McGrath et al. (McGrath et al., 2011), proposed a logarithmic strain energy function as follows:

$$W = -\frac{c_1}{2}\ln(1 - c_2 I_2)$$

where

$I_2 = \lambda_s^2 \lambda_\theta^2 - 1.$

Using the previously described work from Skalak et al. (Skalak et al., 1973):

$$T_s = 2\frac{\lambda_s}{\lambda_\theta}\left(\frac{\partial W}{\partial I_1} + \lambda_\theta^2 \frac{\partial W}{\partial I_2}\right)$$

$$T_\theta = 2\frac{\lambda_\theta}{\lambda_s}\left(\frac{\partial W}{\partial I_1} + \lambda_s^2 \frac{\partial W}{\partial I_2}\right)$$

Then:

$$T_s = T_\theta = 2\lambda_s\lambda_\theta \frac{\partial W}{\partial I_2} = \frac{c_1 c_2 \lambda_s \lambda_\theta}{1 - c_2(\lambda_s^2\lambda_\theta^2 - 1)} + c_3$$

where c_3 is added to allow the unloaded platelet to potentially find an equilibrium under zero tension. In the unloaded state, i.e. with $\lambda_s = \lambda_\theta = 1$, the membrane pre-stress is defined as follows:

$$T_0 = c_1 c_2 + c_3.$$

3.1.4 Problem Space and Solution

Given that the experimental method allows us to measure the deformed platelet geometry (L_p, r_s, R_p) along with the pipette pressure p_i, and atmospheric pressure p_o, the following set of equations needs to be solved numerically for c_1, c_2, c_3, while minimizing the error between modeled and experimental data.

Zone 1:

$$\varphi_1 \leq \varphi \leq \pi \; ; \; \Phi_1 \leq \Phi \leq \pi$$

$$T_\theta^1 = \frac{c_1 c_2 \lambda_s \lambda_\theta}{1 - c_2(\lambda_s^2\lambda_\theta^2 - 1)} + c_3 = \left(\frac{r_s}{2}\right)(p - p_o)$$

$$\lambda_\theta = \frac{r_s \sin\varphi}{R_s sin\Phi}$$

$$\lambda_s = \left(\frac{r_s}{\sqrt{{R_s}^2 cos^2\Phi + {S_s}^2 sin^2\Phi}}\right)\frac{d\varphi}{d\Phi}$$

Zone 2:

$$\varphi = \frac{\pi}{2} \; ; \Phi_3 \leq \Phi \leq \Phi_1$$

$$T_\theta^2 = \frac{c_1 c_2 \lambda_s \lambda_\Theta}{1 - c_2(\lambda_s^2 \lambda_\theta^2 - 1)} + c_3 = \left(\frac{R_p}{2}\right)(p - p_i)$$

$$\lambda_\theta = \frac{R_p}{R_s sin\Phi}$$

$$\lambda_s = \left(\frac{1}{\sqrt{{R_s}^2 cos^2 \Phi + {S_s}^2 sin^2 \Phi}}\right)\frac{dz}{d\Phi}$$

Zone 3:

$$0 \leq \varphi \leq \frac{\pi}{2} \; ; 0 \leq \Phi \leq \Phi_3 \; = \frac{\pi}{2}$$

$$T_\theta^3 = \frac{c_1 c_2 \lambda_s \lambda_\Theta}{1 - c_2(\lambda_s^2 \lambda_\theta^2 - 1)} + c_3 = \left(\frac{R_p}{2}\right)(p - p_i)$$

$$\lambda_\theta = \frac{R_p \sin\varphi}{R_s sin\Phi}$$

$$\lambda_s = \left(\frac{R_p}{\sqrt{{R_s}^2 cos^2 \Phi + {S_s}^2 sin^2 \Phi}}\right)\frac{d\varphi}{d\Phi}$$

The solution procedure starts with calculating the mean cell volume for a given cell, from the volumes calculated from the various aspiration lengths experimentally measured. From this averaged volume, r_s is calculated in Zone 1 for any given pipette pressure, along with the internal cell pressure as

$p = \frac{r_s p_o - R_p p_i}{r_s - R_p}$.

For any given pipette pressure, the procedure to evaluate the deformed geometry can then be started by determining boundary conditions as follows: the points at the bottom and top of the deformed platelet in Fig. 5 lie on the axis of symmetry; therefore, at these points, $\lambda_\theta \cong \lambda_s \; \therefore \lambda = \frac{r_s \, d\varphi}{R_s \, d\Phi} = \frac{r_s \sin\varphi}{R_s \sin\Phi} = K$. For a small deviation α away from the boundary, $\Phi = \pi - \alpha$ and $\varphi = \pi - K_1\alpha$ in Zone 1, and $\Phi = 0 + \alpha$ and $\varphi = 0 + K_3\alpha$ in

Zone 3. This allows the numerical computation of $\frac{d\varphi}{d\Phi}$ at the boundaries, by equating the tension obtained from the equilibrium equation to that obtained from the constitutive equation. Therefore, the stretch ratios in Zones 1 and 3 can be computed numerically using these initial boundary conditions up to Φ_1 and Φ_3 respectively. On the other hand, Zone 2 requires an approximation of λ_s as $dz/d\Phi$ is not defined. Acceptable values for λ_s should be such that the platelet volume is preserved, and as a consequence, should be such that the difference between the longitudinal elongation in Zone 2 and the experimentally measured $L_p - R_p$ are negligible. This is achieved by numerically solving the following equation

$$\left| \int_{\Phi_3}^{\Phi_1} \lambda_s \sqrt{{R_s}^2 \cos^2 \Phi + {S_s}^2 \sin^2 \Phi}\, d\Phi - (L_p - R_p) \right| < \varepsilon,$$

where ε is an acceptable level of error.

3.1.5 MatLab Implementation

MatLab (The MathWorks, Natick, MA) is used to help solve the equations presented in the previous section. To find an optimized set of material constants, global variables R_p, R_s, S_s, V_o, L_p , p_i, p_o, p and r_s are defined in a main program (cteIdent.m) as well as in a separate function (errLC.m) to compute the deformed geometry tensions and strains. The main program uses the built-in *fzero* function to find r_s values for each L_p , p_i pair (corresponding to experimental data points) such that the cell volume remains constant during aspiration ($V_0 \cong V$). The main program then uses the built-in optimising function *lsqnonlin*, with the Levenberg-Marquardt algorithm, to find a set of materiel constants which will return minimal errors between experimental $\left(L_p - R_p\right)$ values and the estimated longitudinal elongations in Zone 2, for all experimental pipette pressures.

The *errLC.m* program uses the built-in *fsolve* function to compute boundary values $\frac{d\varphi}{d\Phi}$ in Zones 1 and 3. It then uses the *ode15i* and *deval* functions to evaluate the values of φ at regular intervals of Φ created using the *linspace* function, with 100 values taken between

the max and min boundaries of Zones 1 and 3, respectively. Φ_1, Φ_3 values are interpolated from φ, Φ pairs using the *interp1* function evaluated at φ_1, φ_3. For Zone 2, the *fsolve* function is used to evaluate the values of λ_s at 100 regularly spaced Φ values between Φ_1 and Φ_3 created using the *linspace* function. The *trapz* function is then used to evaluate the integral

$$\int_{\Phi_3}^{\Phi_1} \lambda_s \sqrt{{R_s}^2 \cos^2 \Phi + {S_s}^2 \sin^2 \Phi}\, d\Phi.$$

3.2 Samples Preparation

Bags of pooled platelets were kindly donated by Dr. Antonio Giulivi from the Ottawa Hospital. These bags contained platelet concentrates collected using automated apheresis techniques including leukoreduction, with approximately 50 mL of ACD-A anticoagulant (Canadian Blood Services, 2014). The bags were gas-permeable; they were stored at 20-24 °C and gently agitated. The bags were transported in a thermally insulated container from the hospital to the research lab, approx. 45 minutes away. Once on site, the bags were placed on an agitating bed again at a room temperature of 20°C, while the experimental setup was prepared.

In compliance with the Tri-Council Policy Statement: Ethical Conduct for Research Involving Humans (TCPS2), given that the platelets originated from multiple, unidentifiable and willing donors, and that the bags were destined for destruction because they had reached their shelf-life limit of 5 days, no ethical review was needed.

When the experimental setup was completed and ready for aspirations, platelet samples were prepared. Platelet concentrate was extracted from the bags using a 10 cc syringe with a 20 gauge needle, and centrifuged (model GS-15R, Beckman Coulter, Mississauga, ON) to pellets at 400 g. Supernatant was removed and the platelets were then suspended in HEPES–modified calcium ions free Tyrode's buffer (138 mM NaCl, 2.7 mM KCl, 2 mM MgCl.6H20, 12 mM NaHCO3, 0.4 mM Na2HPO4, 1% bovine serum albumin, 10 mM HEPES, 5.5 mM dextrose) with Adenosine (5 mM) and Theophylline (3 mM) to prevent platelets activation with contact to foreign surface (J. G. White, Burris, Tukey, Smith 2nd, &

Clawson, 1984). The resulting preparation was then transferred onto a polyethylene glass cover to be observed under the microscope.

3.3 Experimental Setup

All the experiments were run at the Institute for Biological Sciences, National Research Council of Canada, Building M-54, 1200 Montreal Road, in Ottawa, with the kind collaboration of Dr. Geoff Mealing and staff.

3.3.1 Pipettes Preparation

Micropipettes were prepared using a horizontal micropipette puller equipped with a heating square filament of 2.5 mm sides (model P-80, Sutter Instrument Co., Novato, CA). Thin wall glass capillaries, 4 inches long, with 1.5 mm outer diameter, 1.12 mm inner diameter, and with filament (item# TW150F-4, World Precision Instruments Inc., Sarasota, FL) were pulled using the following parameters as read directly on the display of the machine (i.e. units are not specified) (Sutter Instrument, 2015):

Velocity	Pull	Temperature
40	5	690

The resulting pipettes had a long even taper with parallel walls and inner diameters of 0.8-1 µm, adequate to conduct platelets aspirations (Haga et al., 1998; J. G. White et al., 1984). Pipettes tips were filled with HEPES–modified calcium ions free Tyrode's buffer mixed with Adenosine (5 mM) and Theophylline (3 mM) using a 1 cc syringe attached to a filter unit (MILLIPORE, Bedford, MA), and using a thin wire guide (MicroFil 28 g, World Precision Instruments Inc., Sarasota, FL) before being connected to the microelectrode holder. Careful attention was given to ensure no air pockets remained within the micropipettes. A positive pressure was maintained during connection to ensure no air was inadvertently introduced in the system.

3.3.2 Aspiration Setup

The hydraulic system consisted of distilled water in plastic tubing connected to a manometer (catalogue # 33500-082, VWR, Padnor, PA), to a screw-driven 10 cc plastic syringe to control pressure, and finally to a microelectrode holder (World Precision Instruments Inc., Sarasota, FL). Connections in this system were sealed using parafilm ('M' laboratory film, American National Can Company, Chicago, IL). The microelectrode holder was installed in a micromanipulator (model MP-285, Sutter Instrument Co., Novato, CA) to allow for fine movement of the micropipette tip. The setup was kept under a small positive pressure until a sample was ready to be studied to prevent pipette tip blockage.

3.3.3 Imaging Setup

To observe the platelets, an upright microscope (Axioskop FS, Carl Zeiss Inc., Toronto, ON) with phase-contrast optics was used. It was mounted with a Zeiss 100x water dipping objective lens (AchroPlan 100x/1.0 W Ph3, Toronto, ON) and a 10x eyepiece. A video camera (model XCD- X700, SONY, Toronto, ON) connected to a split prism installed on the microscope was used to capture images and to transmit them to a computer running an imaging program (Northern Eclipse, V7.0). The program measurement feature was calibrated using a 1 mm scale with 0.01 divisions (Ted Pella Inc., CA) observed under the microscope. All apparatuses were installed on a hydraulic anti-vibration table (Technical Manufacturing Corporation, Peabody, MA).

3.4 Data Collection

In a typical experiment, the micropipette tip was brought into the platelets preparation under visual control and while maintaining positive pressure to prevent pipette tip blockage. Once focus on the pipette tip was reached, a slight negative pressure was applied until a platelet was captured by the pipette. Image captures where then taken using the computer program at pressure intervals of approximately 1 cmH_2O. These images

captures were then used to measure pipettes internal diameter, length of the platelet lip aspirated (L_p, in Zones 2 and 3), and the diameter of the external spherical portion of the platelet (Zone 1), as per Figure 5. Measurements were carried out once for each data points, using the previously calibrated software measurement features.

4 Results

4.1 Aspirations Imaging

In total, approximately 75 platelets were aspirated following the procedure described above. However, mostly because of platelet activation, only five experiments (*n*=5) were amenable to the desired image processing and analysis. Figure 6 presents an example of such data. Measurement precision was set to 0.02 µm as a result of image clarity limits. It was observed that the protruding portion of the platelets did not always remain spherical; the differences between minimum and maximum diameters increased with increasing aspiration pressure. For consistency with the theoretical model, the minimum and maximum diameters observed were averaged to provide an estimated spherical diameter.

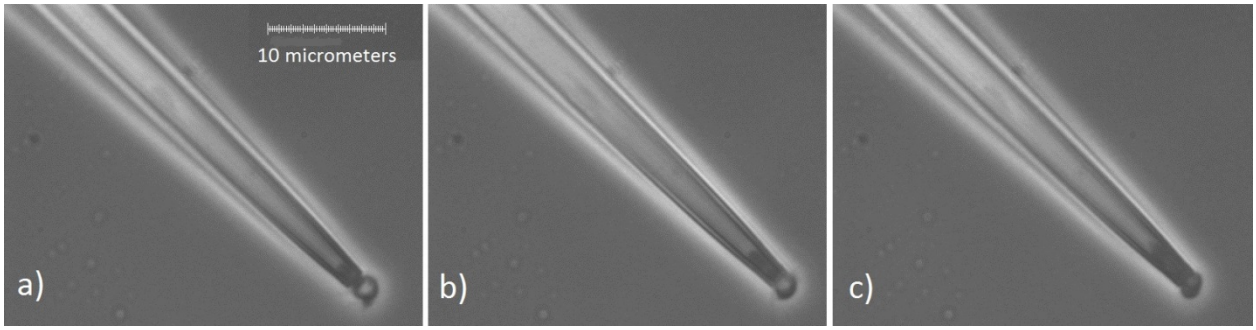

Figure 6. Platelet aspiration at aspiration pressures of a) 2.1, b) 3.0, and c) 4.1 cmH_2O respectively.

Figure 7 is a zoomed-in portion of background platelets in suspension, in which activated platelets can be identified by their pseudopods extensions. Activated platelets could be observed in the background during all the experiments. Platelets at this stage of activation could also be seen when platelet rich plasma was taken from the bags and observed directly, with or without the use of Tyrode's buffer, and with or without the use of adenosine and theophylline.

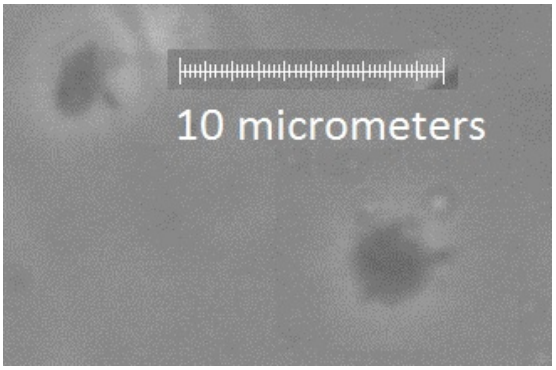

Figure 7. Background platelets in suspension during the manipulations. They consistently showed some level of activation, albeit small.

4.2 Elongation-pressure Data

Table 1 presents the initial time-varying response of two sample platelets immediately following aspiration under constant negative pressure. The initial elongation was followed by a quick retraction and slow creep until the 30 seconds mark. Therefore, in the rest of the experiments, elongation measurements were taken once equilibrium was reached, around the 30 seconds mark.

Table 1. Platelet aspiration lengths under constant pressure. P: aspiration pressure, L_p: aspirated length, t: time under aspiration.

Sample ID	***P*** **[±0.1 cmH_2O]**	***L_p*** **[±0.02 µm]**	***t*** **[±.5 s]**
1-23SepA20	-5.0	3.66	0
1-23SepA21	-5.0	3.29	7
1-23SepA23	-5.0	3.65	22
1-23SepA24	-5.0	3.65	32
2-23SepA26	-6.0	4.06	0
2-23SepA27	-6.0	3.92	9
2-23SepA30	-6.0	3.97	28
2-23SepA31	-6.0	4.28	58

Figure 8 presents pipette radius normalized elongation-pressure data obtained from five different human platelets (most likely from five different donors) by micropipette

aspiration. Normalization is useful given the different pipette radii achieved by pulling, as new pipettes were used for each experiment. Although the data in Figure 8 seem to separate into two distinct groups, no statistically significant conclusions could be drawn due to the small sample size.

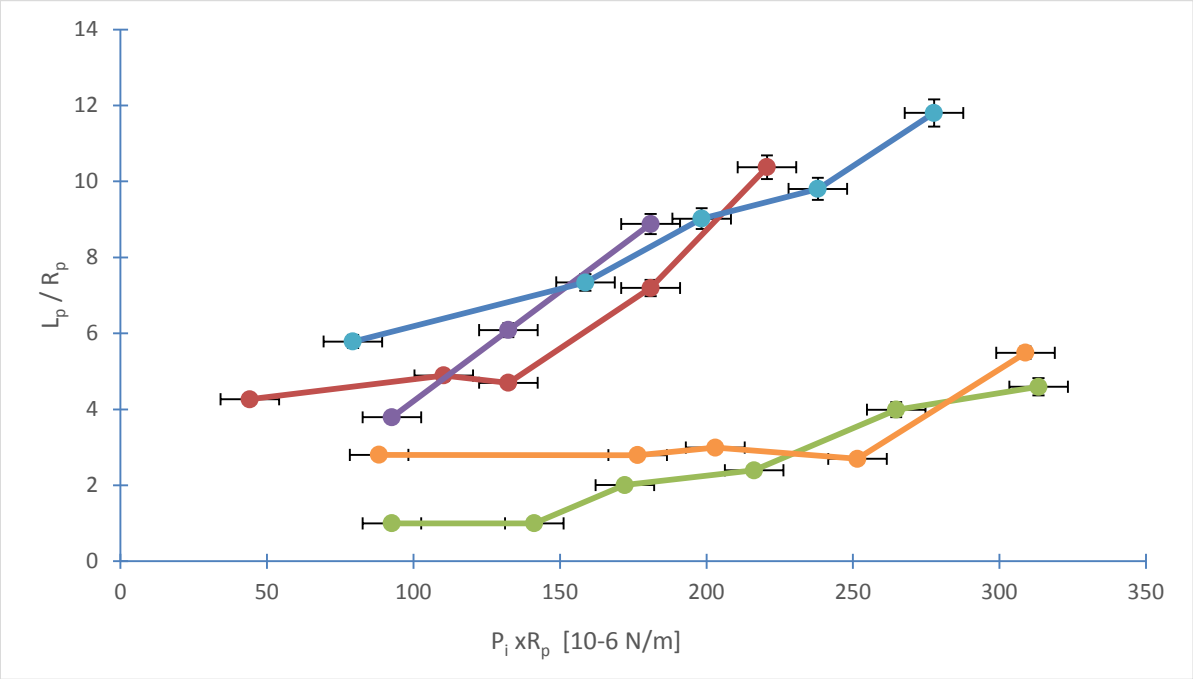

Figure 8. Normalized elongation-pressure data for five individual human platelets undergoing micropipette aspiration. One color corresponds to one platelet. L_p: aspirated length (µm), R_p: pipette radius (µm), P_i: aspiration pressure (Pa).

The data in Figure 8 was then averaged for all tested platelets by pressure intervals of 1 through 4 cmH_2O, to produce the plot in Figure 9. The resulting data set shows strong linear correlation (R^2 = 0.92) between the averaged normalized elongation and pressure, and the regression analysis demonstrates that both the slope and intercept are statically significant (P_a = 0.0026; P_b = 0.0129).

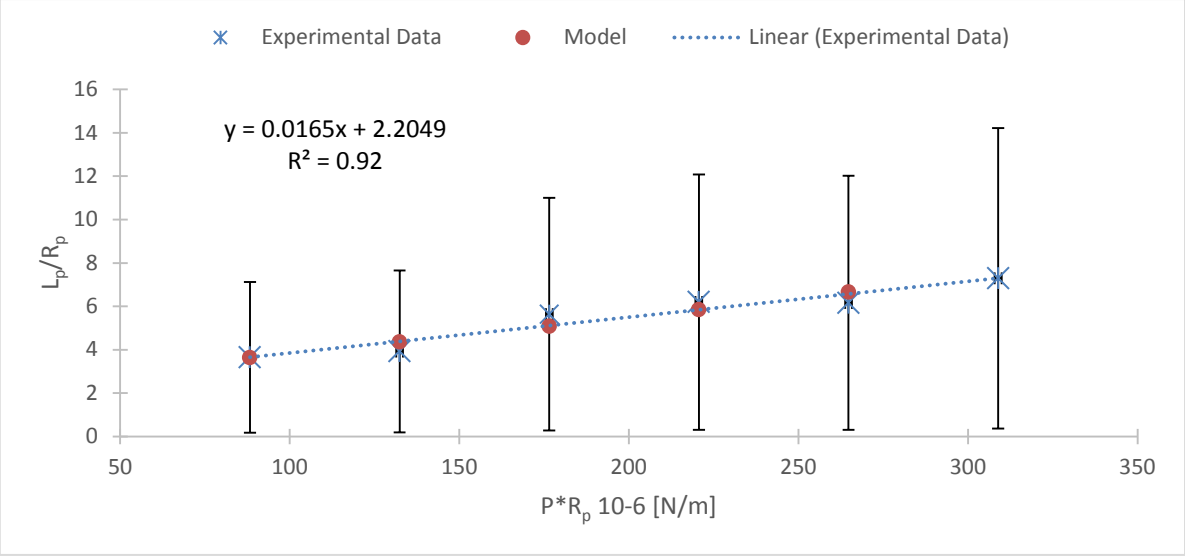

Figure 9. Average elongation-pressure behaviour for five human platelets. Model predictions (solid circles) replicate the linear fit of average experimental data (stars). L_p: aspirated length (µm), R_p: pipette radius (µm), P: aspiration pressure (Pa).

4.3 Model Predictions

4.3.1 Platelet Volume

Table 2 presents the average cell volume for each of the five platelets when they were submitted to a range of aspiration pressures or 4 to 5 points (1 cmH_2O – 4 or 5 cmH_2O). Given the assumptions of constant volume (i.e. barring leakage of cytoplasm through the membrane and/or rupture of the membrane) and the proposed deformed platelet geometry, the calculated cell volume varied between 5.4 and 7.1 x 10^-18 m^3.

Table 2. Calculated average human platelet volume based on constant volume assumption and proposed deformed geometry; n=5.

Data ID	Average Volume ± SD [10^-18 m^3]
1-14OctA	5.4 ± 0.6
2-14OctC	5.4± 0.4
3-14OctE	7.0 ± 1.2
4-14OctF	5.4 ± 0.6
5-23SepA	7.1± 1.6
Average	6.1 ± 0.9

4.3.2 Platelet Deformation

The left column of Figure 10 presents the predicted platelets deformation under aspirations ranging from 1-4 cmH_2O using the material constants obtained from the averaged experimental data. The deformed platelet shrinks circumferentially while elongating in the meridional direction, with a peak meridional stretch at the pipette entrance, as seen in the middle column of Figure 10. The top and bottom points of the platelet do not undergo any deformation as per model assumptions.

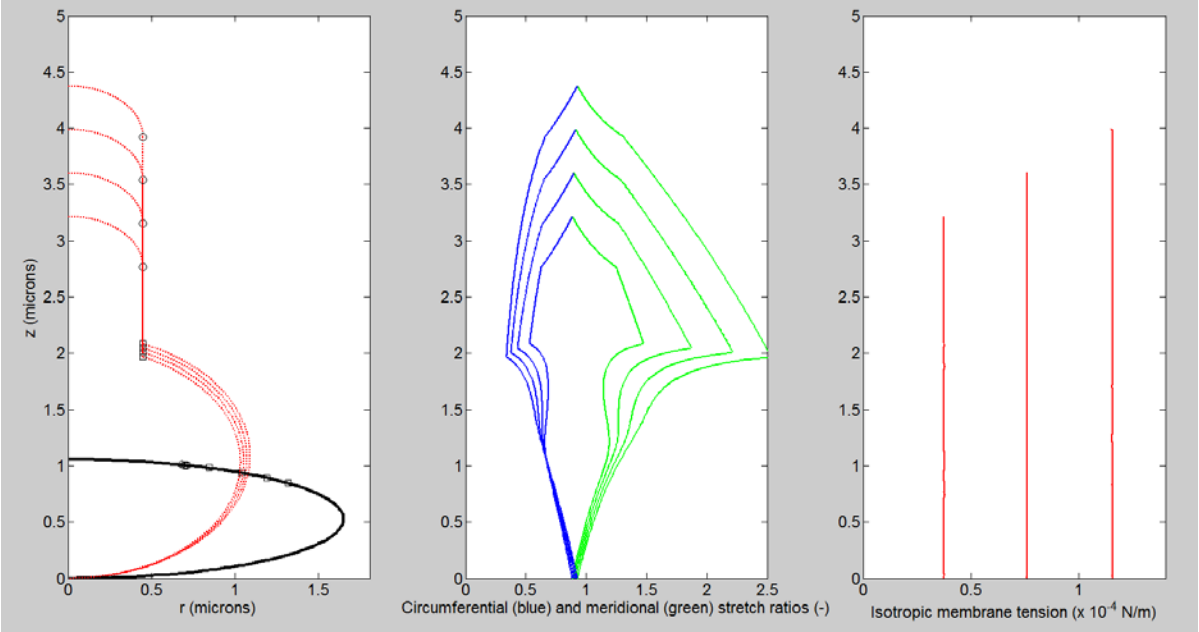

Figure 10. Simulated aspiration experiment over 1-4 cmH_2O range using the material constants obtained from the averaged experimental data. Left column: initial (black) and deformed (red) geometries – the dots identify the extremal contact points between the platelet and the pipette in the initial and deformed shapes; Middle column: circumferential (blue) and meridional (green) stretch ratios; Right column: isotropic membrane tension

4.3.3 Membrane Tension

The right column of Figure 10 shows the simulated isotropic membrane tension under aspirations ranging from 1-4 cmH_2O using the material constants obtained from the averaged experimental data. The membrane tension increases linearly as aspiration pressure increases, and ranges from ~ 0.4 to 1.55 x 10^{-4} N/m.

4.3.4 Influence of Volume on Mechanical Properties

Table 3 presents the materiel constants obtained for different platelets volumes using the experimental linear elongation-pressure relation from Figure 9. The value of constant c_1 increased with the platelet volume while that of c_2 decreased, and that of c_3 remained

stable. The platelet membrane pre-stress T_0 did not significantly change with platelet volume.

Table 3. Materiel constants derived from experimental averaged deformations, with various platelet volumes.

Volume [10^{-18} m^3]	Constants [± 95% Confidence Interval]			
	c_1 [N/m]	c_2 [10^{-4}]	c_3 [10^{-3}]	T_0 [10^{-4} N/m]
5.38	5.023 ± 0.001	3.08 ± 0.08	-1.31 ± 0.04	2.3 ± 0.8
6.05	5.435 ± 0.005	2.83 ± 0.04	-1.30 ± 0.02	2.4 ± 0.5
7.05	5.983 ± 0.001	2.59 ± 0.04	-1.30 ± 0.02	2.5 ± 0.5

Figure 12 presents the simulated elongation-pressure behaviour of the same five human platelets as in Figure 9, based on an arbitrarily wide range of platelet volumes. Elongation increases with platelet volume.

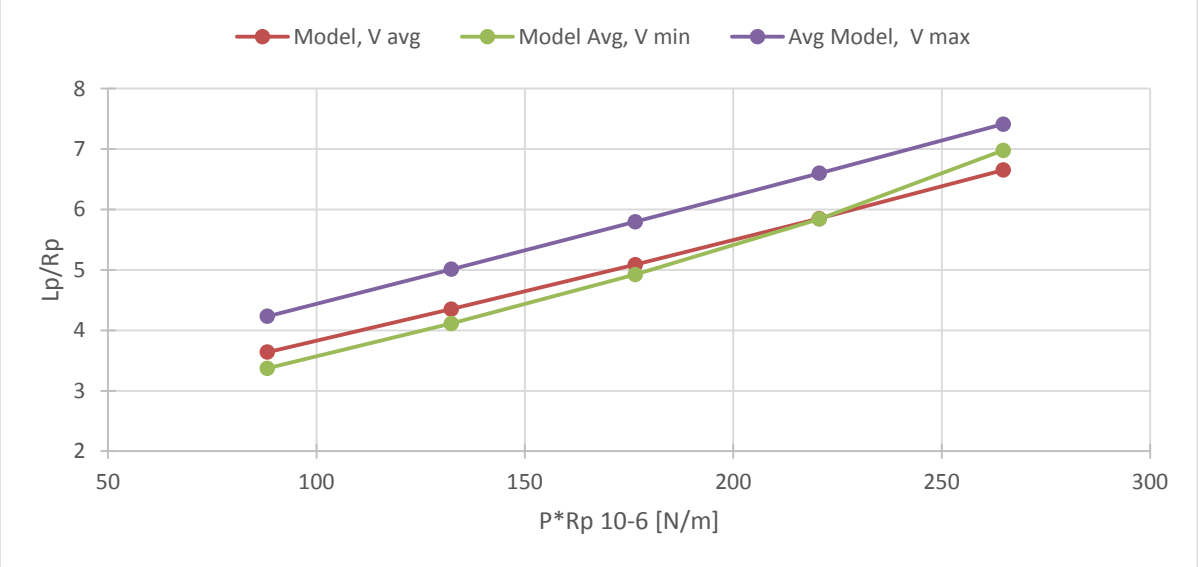

Figure 11. Simulated elongation-pressure behaviour of human platelets for V_{min} = 4E-18 m^3, V_{avg} = 6.05E-18m^3, and V_{max} = 10E-18m^3, based on experimental material constants. L_p: aspirated length (µm), R_p: pipette radius (µm), P_i: aspiration pressure (Pa). Note that no error bars are indicated because the curves were obtained from simulation.

4.3.5 Influence of Initial Platelets Shape Ratio on Mechanical Properties.

Table 4 presents the material constants obtained for different shape ratios using the experimental linear elongation-pressure relation from Figure 9. Constant c_1 and membrane pre-stress T_0 values increased with decreasing shape ratios. Figure 13 presents modeled elongation-pressure variations with shape ratio. Overall, decreasing initial shape ratios results in increased elongations.

Table 4. Material constants derived from experimental averaged data, for various oblate spheroid shape ratios.

Shape Ratio	Constants			
	c_1 [N/m]	c_2[10^{-4}]	c_3 [10^{-3}]	T_0 [10^{-4} N/m]
0.24	6.686 ± 0.008	2.62 ± 0.02	-1.30 ± 0.01	4.5 ± 0.3
0.32	5.435 ± 0.005	2.83 ± 0.04	-1.30 ± 0.02	2.4 ± 0.5
0.40	5.032 ± 0.004	2.81 ± 0.01	-1.30 ± 0.01	1.1 ± 0.2

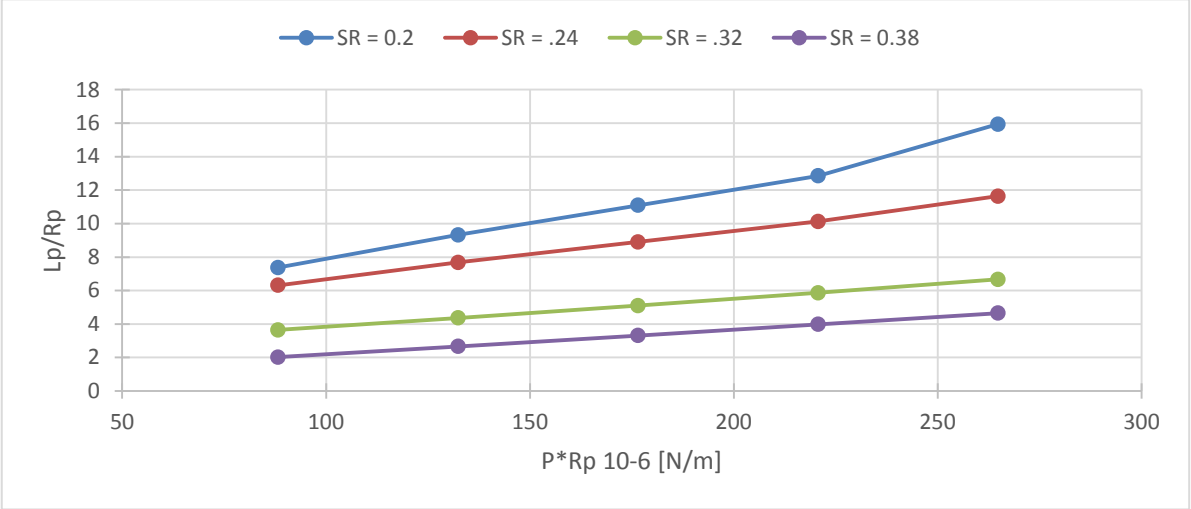

Figure 12. Model elongation-pressure predictions for various underformed oblate spheroid shape ratios, based on experimental averaged material constants. L_p: aspirated length (µm), R_p: pipette radius (µm), P_i: aspiration pressure (Pa). Note that no error bars are indicated because the curves were obtained from simulation.

5 Discussion

5.1 Aspirations Imaging

The images collected indicated that the external portion of the platelets did not remain spherical as previously reported (McGrath et al., 2011; J. G. White et al., 1984). This could be explained by the activated state of the platelets, which is evident in Figure 7, where the aspirated platelet seems to reorganize its cytoskeleton to likely wrap around the pipette surface. This effort is however counteracted by the aspiration pressure and by the use of calcium reducing inhibition agents, which limit the platelet's potential to contract. Activated platelets were observed across various preparation methods: in preparations with or without inhibition agents, in preparations where platelets were only washed with Tyrode's buffer, and in unmodified pooled platelet samples taken directly from the bag. These observations suggest that the removal process from the bags using a 20 gauge needle likely induced activation, and would support the recommendation not to use smaller than 19 gauge needles when handling platelets to prevent platelets activation (Gibbins & Mahaut-Smith, 2004). Other factors that could have contributed to platelets activation are: insufficient washing and precautions to ensure all traces of thrombin were removed from the platelets samples; high vacuum during retrieval of platelets samples from bags; and radiating heat arising from the microscope lighting system.

5.2 Elongation-pressure Data

The observed deformability response changed significantly from platelet to platelet. This may be explained in large portion by the intrinsic variability in platelets properties (Haga et al., 1998; Michelson, 2006), but also to some extent by the experimental method, as the platelets seemed to be activated. First, platelets activation could be expected to translate into increased deformability, given that the function of platelet activation is to allow it to cover an injured area, and to extend pseudopods to grab onto other platelets. However, this evolution might be countered by the internal contractile forces generated by

the cytoskeleton trying to engulf the micropipette. In addition, these effects are likely modulated by the degree of effectiveness of the inhibiting agent on individual platelets and/or manipulations from one suspension to the next.

The initial elongation and quick retraction upon pressure change may be explained by the experimental setup having a stabilisation time due hydraulic flow and air compression at the manometer interface with the hydraulic system. The slow creep phase may be indicative of the previously reported viscoelastic behaviour of platelets (Haga et al., 1998). Another possible contributor might be a possible reactive response of the platelet to mechanical stimuli, contracting or "absorbing" the deformation via the movement of glycoproteins on its membrane.

The averaged deformation data suggested a linear relationship between the pipette radius normalized aspiration lengths and the aspiration pressures, as previously reported (Haga et al., 1998; McGrath et al., 2011). Both the slope, of 16.5 $(dynes/cm)^{-1}$, and intercept, of 2.2 (dimensionless), obtained for this experiment, are higher than the slope of 10.4 $(dynes/cm)^{-1}$, and intercept of 0.97 (dimensionless) reported by Haga et al. (Haga et al., 1998). As previously discussed, this could be explained both by the increased deformability of activated platelets, and simply by the variability in individuals platelets properties given the small sample size.

5.3 Model Predictions

The material constants obtained, c_1= 5.435 ± 0.005 N/m , c_2= (2.83 ± 0.04) x 10^{-4}, and c_3 = (-1.30 ± 0.02) x 10^{-3} , while different from those obtained by McGrath et al., 2011, (c_1= 5.100 N/m , c_2= 4.97 x 10^{-4}, and c_3 = -2. 014 x 10^{-3}, modeled from human platelets elongation data reported by (Haga et al., 1998), are in agreement in term of signs and scales. The difference could be explained by the use of an assumed average volume of 7.3 fL by McGrath et al., 2011 since this data was not reported by (Haga et al., 1998). Numerical methods could also be a factor in constants variation due to the different versions of MatLab and computing platforms used. Again, platelets activation state and inherent variability also influence the material constants variation.

5.3.1 Platelets Volume

The calculated experimental volumes fall within the reported normal range of values for human platelets (Gulcan, Varol, Etli, Aksoy, & Kayan, 2012; Michelson, 2006), however some individual platelets show volumes below the normal range of 6-10 fL. This conflicts with previously reported increase in platelets volume with the change in shape from the discoid to the spheroid conformation (Laufer, Grover, Ben-Sasson, & Freund, 1979). The most significant contributor to volume discrepancies would be the averaged major and minor radiuses applied to experimental values to approximate a spherical radius for Zone 1. Again, due to activation, Zone 1 for aspirated platelets did not remain spherical with ratio between major and minor radii ranging between 1 and 1.3 on average, and with some up to 1.6.

Another contributing factor to volume discrepancies is the α-granules secretion as part of platelets activation sequence. α-granules account for 10% of platelets volume (Flaumenhaft, 2013), and could explain the volume reduction for the observed platelets undergoing aspiration. Also, since the platelets cytoplasm is essentially solid struts of actin in a liquid gel-like substance, this structure may likely be broken and compressed, leading to reduced volume during aspirations. A supporting rationale for this argument is that during activation, the synthetized cAMP molecules enable platelets remodeling by breaking actin filaments which can then be reassembled (Hartwig, 2013). Also in support of the reduced volume of activated platelets, a recent detailed study of resting (n=1883) and activated (n=2050) platelets demonstrated that the average platelet sees its volume drop from 10 fL to 9.4 fL, while its shape ratio goes from 0.29 to 0.44 from the resting to the activated state (Moskalensky et al., 2013).

5.3.2 Platelets Deformation

The model accurately reproduces averaged experimental aspirated lengths based on linear approximation presented in Figure 9. However, it is important to note the significance of using averaged versus individual elongation-pressure behaviours. Linear fits

to the individual elongation-pressure behaviours (i.e. for one platelet under a range of aspiration pressures) presented in Figure 8 result in R^2 values of 0.47 to 1, while a linear fit to all five platelets results in a R^2 value of 0.1, highlighting a weak correlation over the platelet population. What was done instead in Figure 9 is that the data points were

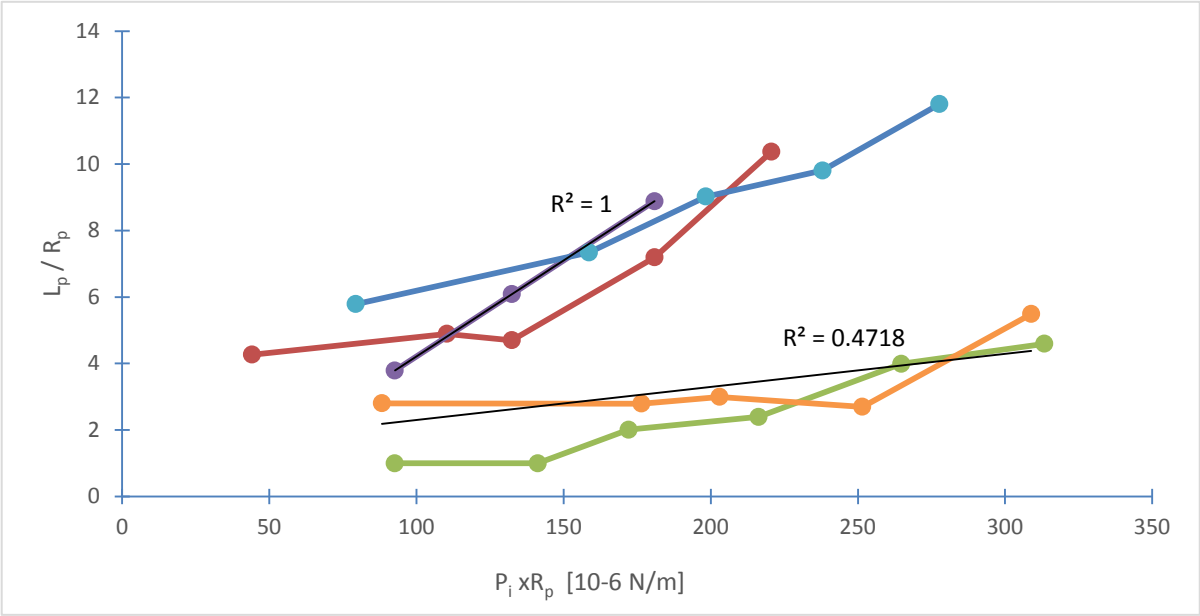

Figure 13 (Reproduced for convenience). Experimental elongation-pressure behaviours for five human platelets undergoing micropipette aspiration, with tentative individual linear fits. For clarity, only the worst and best fits are shown.

averaged first (say, at a given aspiration pressure), and the linear fit was done thereafter.

As such, model predictions should not be used to identify specific elongation-pressure values, but rather for trends and general relations between its variables. This issue is further exacerbated by the fact that the model provides a very simplistic relation between strain energy and membrane stresses in two dimensions over the surface of the platelet. It does not account for the complexity of the platelets structure and underlying varying material properties.

5.3.3 Membrane Tension and Strain

Given the model geometric assumption that both Zones 1 and 3 are spherical, and that the platelet is a homogenous material, isometric tension is expected across the platelet during aspiration. It is interesting to note its linear increase with aspiration pressure. This is expected from the development of the geometry and equilibrium equations that constrain the solution to be linear ($T = k\Delta p$) and by the isotropic material assumption. The fact that the rupture point of the platelet membrane under high aspiration pressure occurs at the interface between the micropipette tip and the platelet (Haga et al., 1998), where the model predicts the greatest meridional stretch ratio, suggests that the failure mechanism may be triggered by strain rather than stress.

5.3.4 Influence of Volume on Mechanical Properties

Volume was shown not to significantly affect membrane pre-stress (Table 3). This is in agreement with the literature as pre-stress has been described as a function of the microtubule coil around the equatorial plane of the resting platelet. This may imply that the circumferential platelet microtubule is assembled to give the platelets a certain shape ratio and therefore a certain pre-stress. This in turn would suggests that the microtubule coil would not be ssembled to attain a pre-determined length, but rather be assembled to meet a certain stress threshold between the platelet membrane and the coil. Cell deformability did not significantly vary with platelet volume as seen in Figure 12. However, when the platelet volume was reduced below the experimental average, the elongation-pressure relationship did not remain linear. This could be explained by a departure from elastic behaviour at higher stretch ratios, or by the model inaccuracy outside a certain range of parameters.

5.3.5 Influence of Initial Platelets Shape Ratio on Mechanical Properties.

Variations in the undeformed platelet shape ratio significantly affected membrane pre-stress values as identified in Table 4. This is in accordance with theory, as without the

microtubule coil, the rested platelets would be spherical, implying that the coil pushes radially on the membrane to give its oblate geometry. Therefore, the greater the difference between the meridional radius and the equatorial radius, the greater the stress applied by the coil to deform the platelet. This aspect alone comes as a strong support for the validity of the proposed model.

5.4 Contributions, Limitations and Future Work

The work presented in this thesis serves to highlight the complexity of platelets study. Manipulations of platelets are notably difficult for the purpose of mechanical testing, and extreme care and attention to details is required in the selection of inhibiting agents, the tools used to prepare samples, and the observation methods. Although previously reported methods were followed, minor details which were not described in these methods, were significant enough to cause platelets activation throughout all experiments, even after numerous hours trying slightly different manipulations to identify the source of activation. Experimental results for platelets deformation are similar to those obtained by (Haga et al., 1998), although platelets observed were activated. This reinforces the observed linear relationship between elongation and pressure for platelets undergoing large deformations.

The presented model contributes to a better understanding of the platelets macro deformations within a limited pressure range. It indicates that the platelet's initial shape ratio has a significant influence on the resulting mechanical properties and deformability, while the platelet's volume would not significantly contribute to its deformability. It also suggests that the observed platelet rupture reported by (Haga et al., 1998), would occur due to strain. The model also accurately simulates experimental human platelets elongations over a range of pressures during micropipette aspiration.

However, the present work is limited by the simplification brought in by forces acting in 2 dimensions along the surface of the cell. Future models need to consider the platelet's solid-gel cytoskeleton in the distribution of stresses and strains. Also, the suggestion that the platelet's undeformed shape ratio significantly influences its mechanical properties opens up interesting areas for further exploration. Aspiration measurements on platelets

whose shape ratios were previously recorded would clarify if this proposition is valid or not. Another clear limitation that applies to any in-vitro study, but most of all to such a reactive system as the platelet, is the translation of experimental findings to in-vivo applications. The platelet being very sensitive, mechanical interactions with it will continue to require severe inhibitory precautions which alter its mechanical properties. To overcome this physical interaction, the optical stretching method should be explored to see its applicability to platelets, as it would allow measurement of stresses required to activate platelets without contact with a foreign substance. The optical stretching method would also allow to overcome another limitation of the micropipette aspiration technique; it would allow a finer force gradient to be applied on the cell instead of coarse step increases. Removing the direct mechanical contact and finer resolution of applied forces would enable the measurement of the required forces to activate a platelet.

6 Conclusion

Cellular mechanics has been an extremely active and developing field over the last two decades. Significant advances in biology-related mechanics have been made. However, the complexity and reactivity of living organism remain a significant challenge in terms of modeling. This thesis describes an approach to understand platelets mechanics from a holistic, whole cell perspective, and provides modelling and theoretical foundations to build an increasingly accurate model, which would account for sub-structures. Ji and Bao (Ji & Bao, 2011) have put forward a fundamental paradox that very well describes the situation of the researcher trying to draw conclusions on the platelets mechanical properties: “How can we measure mechanical behavior of living cells if they react to the measurement tools?”

Appendix A: Commented MatLab Code

Material Constants Optimisation MatLab Code (cteIdnt.m)

The following code is the implementation of a micropipette aspiration constitutive model described in the thesis work submitted by Mathieu Sayeur (2015) in partial fulfillment of the MASc Biomedical Engineering degree at University of Ottawa.

Variables Initiation

Clears the MatLab workspace and sets the default output format to a scaled fixed point format with 5 digits before setting global variables.

```
clc
clear
format short

global rp rrs ss lpexp ppi ppo pp rs
```

Where:

- *rp* is the pipette radius, in meters
- *rrs* is Rs, the undeformed equatorial radius, in meters
- *ss* is Ss, the undeformed meridional radius, in meters
- *lpexp* is the experimental Lp value measured, in meters
- *ppi* is the aspiration pressure inside the pipette
- *ppo* is the ambiant pressure, 101.3 kPa
- *pp* is the platelet internal pressure
- *rs* is the deformed equatorial radius

Experimental Data Input

Textscan reads data from an open text file identified by FID into cell array C.

Format the text file 'mydata.txt' as follows: First line is [*rp*, *vO*], units are [m, m^3] Each following line is a [*p*, *Lp*] experimental data point, units are [cmH2O, m]

```
  0.45E-6    6.05E-18
  1          1.12906E-06
  1.5        1.34215E-06
  2          1.55523E-06
  2.5        1.76831E-06
  3          1.98139E-06
 [...]
```

Where:

- *v0* is the volume of the rested platelet in cubic meters,
- *deltapexp* is the experimental aspiration pressure in centimeters of water, converted to pascals.

```
fid = fopen('expAllavg.txt', 'rt');

    c = textscan(fid, '%f %f',1);
    rp = c{1};
    v0 = c{2};

    c = textscan(fid, '%f %f');
    deltapexp = c{1};
    deltapexp = deltapexp.*98.067;
    lpexp = c{2};

fclose(fid);
```

Variables Definitions

The following section calculates and defines the required variables to compute the material constants.

```
shaperatio = 0.32;
```

shaperatio is the ratio of the rested platelet *ss/ rrs*

```
ppo = 101300.*ones(length(lpexp),1);
```

Initializes room pressure as an array the same lengths as the number of experimental values inputted, with 101300 Pa values.

```
ppi = ppo - deltapexp;
rrs = (3*v0/(4*pi*shaperatio))^(1/3);
```

Calculates rrs using the averaged experimental platelet volume inputted in the following equation:

$$S_s = \left(\frac{3V_o}{4\pi(SR)}\right)^{\frac{1}{3}}$$

```
ss = shaperatio*rrs;
iniconstants=[5.0 1.0e-4 -3.8e-4];
```

iniconstants is an initial guess for material constants.

```
rs=zeros(length(lpexp),1);
```

Initializes rs as an array the same lenghts as the number of experimental values inputted, with zero values.

```
warning off all;
```

Prevents the displays of warning across any functions which uses warnings.

Material Constants Optimization

The following for loop identifies a calculated value of rs which conserves volume for each experimental [*p*, *Lp*] data point input, using the fzero function with the following options:

- 'TolX',1e-20 sets the termination tolerance on x, the current point, at 1e-20.
- 'tolFun',1e-32 sets the termination tolerance on the function value at 1e-32.
- 'Display', 'off'displays no output for the fzero function.

`fzero(f,rrs,optionsfzero);`

tries to find a zero of the function *f* starting near rrs. The value X returned by FZERO is near a point where FUN changes sign. Where *f* is:

$$f = V_0 - \left(\frac{4}{3}\pi {r_s}^3 - \frac{\pi}{3}\left(r_s - \sqrt{{r_s}^2 - {R_p}^2}\right)^2\left(2r_s + \sqrt{{r_s}^2 - {R_p}^2}\right) + \pi\left(L_p - R_p\right){R_p}^2 + \frac{2}{3}\pi {R_p}^3\right)$$

```
for i=1:length(lpexp)
 f = @(x) v0 - pi.*(4./3.*x.^3 - 1./3.*(x - sqrt(x.^2 - rp.^2)).^2.*(2.*x + sqrt(x.^2 -
rp.^2)) + 2./3.*rp.^3 + (lpexp(i) - rp).*rp.^2);
 optionsfzero = optimset('TolX',1e-20,'TolFun',1e-32, 'Display', 'off');
 rs(i) = fzero(f,rrs,optionsfzero);
end

pp = (ppo.*rs-ppi.*rp)./(rs-rp);
```

Evaluates the internal platelet pressure, used in errLC.

```
options = optimset('MaxFunEvals',1e100,'tolFun',1e-10,'TolX',1e-
10,'MaxIter',5e3,'Algorithm','levenberg-marquardt');
```

options = optimset sets options for nonlinear optimization as follows:

- 'MaxFunEvals',1e100 sets the maximum number of function evaluations allowed to 1E100,
- 'tolFun',1e-10 sets the termination tolerance on the function value at 1e-10
- 'TolX',1e-10 sets the termination tolerance on x, the current point, at 1e-10
- 'MaxIter',5e3, sets the maximum number of iterations allowed to 5e3
- 'Algorithm','levenberg-marquardt' sets the optimisation algorithm as the levenberg-marquardt with lambda = 0.01 (default)

Optimisation of materiel constant as defined in errLC is done using the lsqnonlin function:

```
lsqnonlin(@errLC,iniconstants,[],[],options);
```

It solves the non-linear least squares problem errLC using initial constants as defined in initconstants and using the options mentioned above, and without upper or lower bounds.

It returns [Constants,resnorm,residual,exitflag,output,l,J] where:

- *Constants* is the optimzed set of contants [c1, c2, c3]
- *resnorm* returns the value of the squared 2-norm of the residual at X: sum(errLC(X).^2)
- *residual* returns the value of the residual at the solution X: RESIDUAL = errLC(X)
- *exitflag* returns an EXITFLAG that describes the exit condition of LSQNONLIN.
- *output* returns a structure OUTPUT with the number of iterations taken in
- OUTPUT.iterations, the number of function evaluations in
- OUTPUT.funcCount, the algorithm used in OUTPUT.algorithm, and the exit message in OUTPUT.message.
- *l* returns the set of Lagrangian multipliers, LAMBDA, at the solution: LAMBDA.lower for LB and LAMBDA.upper for UB
- *J* returns the Jacobian of errLC at *constants*

```
[Constants,resnorm,residual,exitflag,output,l,J]=...
lsqnonlin(@errLC,iniconstants,[],[],options);
```

The section below prints the results of the optimisation and its 95% confidence interval using the nlparci function with the Jacobian from the lsqnonlin function.

```
fprintf('\n');
fprintf('MODEL CONSTANTS\n');
CI = nlparci(Constants,residual,'jacobian',J);
fprintf('c1 = %12.4g +/- %12.4g\n',Constants(1),0.5*(CI(1,2)-CI(1,1)));
fprintf('c2 = %12.4g +/- %12.4g\n',Constants(2),0.5*(CI(2,2)-CI(2,1)));
fprintf('c3 = %12.4g +/- %12.4g\n',Constants(3),0.5*(CI(3,2)-CI(3,1)));
```

Material Constant Optimisation MatLab Code (errLC.m)

The following code is called in the cteIdnt.m file. It serves as the non-linear problem which requires to be optimized to reduce the error between modeled deformation and experimental data. Its inputs are materiel constants c=[c1,c2,c3] and global variables, and it returns the difference between the modeled and the experimental deformation value.

```
function error=errLC(C)
```

Variables Initiation

```
global rp rrs ss lpexp ppi ppo pp rs
```

Declares global variables, values from main program file cteIdnt.m

```
c1 = C(1);
c2 = C(2);
c3 = C(3);
```

Assigns material constants as per the defined energy-strain function:

$$W = -\frac{c_1}{2}\ln(1 - c_2 I_2)$$

```
resolution = 100;
```

resolution is used to set the number of points evaluated by the model between known boundaries.

```
eps = 1e-10;
```

eps is ε, the value of the distance away from the axis of rotation, the initial boundary, used to define the initial value of the derivative of $\frac{d\varphi}{d\Phi}$.

```
options1 = optimset('TolX',1e-12,'TolFun',1e-20, 'Display', 'off');
options2 = odeset('RelTol',1e-6,'AbsTol',1e-6);
```

options1 is the set of options used in *fsolve*. *options2* is the set of options used in *ode15i*.

Zone Analysis

The remainder of the code goes through each zones to solve stretch ratios as per model definitions, where variable are defined as follows:

- *yp##* is differential $\frac{d\varphi}{d\Phi}$.
- *t#s* is Φ#, the zone 2 boundaries rested geometry Φ angles.
- *t0#* is Φ at initial boundary condition, $\Phi = \pi - \varepsilon$
- *y0#* is φ at initial boundary condition $\varphi = \pi - \frac{d\varphi}{d\Phi}\varepsilon$,
- *tspan1* is that span of the linear space, i.e. boundaries between which *resolution* is applied.
- *t#* is a linear space of *resolution* points
- *y#* is φ
- *y#s* is φ#, the zone 2 boundaries deformed geometry φ angles.
- *odefun#* refers to a set of equations which describes the equilibrium state

Zone 1: External Sphere

```
yp01 = zeros(length(lpexp),1);
t1s = zeros(length(lpexp),1);
```

Variables initilizations.

```
for j = 1:length(lpexp)
 yp01(j) = fsolve(@fun1,2,options1);
end
```

- This for loop solves the value of $\frac{d\varphi}{d\Phi}$ for each experimental data points. Zone dependant equilibrium equations allows to solve $\frac{d\varphi}{d\Phi}$ and are defined in *fun#* functions at the end of this code.

```
t01 = pi-eps;
y01 = pi-yp01.*eps;
tspan1 = [t01,0];
```

```
for j = 1:length(lpexp)
 sol1 = ode15i(@odefun1,tspan1,y01(j),yp01(j),options2);
 t1 = linspace(min(sol1.x),max(sol1.x),resolution);
 y1 = deval(sol1,t1,1);
 y1s = asin(rp/rs(j));
 t1s(j) = interp1(y1,t1,y1s);
end
```

This *for* codes evaluates φ at any point defined in *t1* the linear space between max/min values of Φ. It then interpolates Φ_1 value from φ_1 . The *ode15i* function is used to solve the fully implicit differential equation:

$$0 = r_s(p - p_o) - \frac{c_1 c_2 \lambda_s \lambda_\theta}{1 - c_2(\lambda_s^2 \lambda_\theta^2 - 1)} - 2c_3$$

Zone 3: Internal Hemisphere.

```
yp03 = zeros(length(lpexp),1);
t3t = t1s;
for j = 1:length(lpexp)
 yp03(j) = fsolve(@fun3,1,options1);
end
y03 = yp03.*eps;
tspan3 = [eps,pi];
for j = 1:length(lpexp)
 sol3 = ode15i(@odefun3,tspan3,y03(j),yp03(j),options2);
 t3 = linspace(min(sol3.x),max(sol3.x),resolution);
 y3 = deval(sol3,t3,1);
 y3t = pi/2;
 t3t(j) = interp1(y3,t3,y3t);
end
```

Same explanations as Zone 1.

Zone 2 : Cylinder

```
error = zeros(length(lpexp),1);
for j = 1:length(lpexp)
```

```
     t2 = linspace(t3t(j),t1s(j),resolution);
     ls2 = ones(1,resolution);

     for i =1:resolution
        lt2 = rp/(rrs*sin(t2(i)));
```

```
        ls2(i) = fsolve(@fun2,1,options1);
 end
```

Evaluates stretch ratios at each point in linear space of *resolution* between zone 2 Φ_1, Φ_3 boundaries.

```
int2 = trapz(t2,ls2.*sqrt((rrs.*cos(t2)).^2+(ss.*sin(t2)).^2));
error(j) = (lpexp(j)-rp-int2)./(lpexp(j)-rp);
```

The output *error* is the difference between the experimental aspiration length and the calculated value. *int2* is the model calculated dz based on model, and s done so by the trapezoidal integration of the following equation between zone 2 Φ_1, Φ_3 boundaries.

```
End
```

```
function                        f1                        =                        fun1(x)

 f1 = (pp(j)-ppo(j))*rs(j) - (2*c1*c2*((rs(j)/rrs)*x)^2)/(1-c2*(((rs(j)/rrs)*x)^4-1)) - 2*c3;

end
```

```
function                        f2                        =                        fun2(x)

 f2  =  (pp(j)-ppi(j))*rp  -  (2*c1*c2*((rs(j)/rrs)*x)^2)/(1-c2*(((rs(j)/rrs)*x)^4-1))  -  2*c3;

end
```

```
function                        f3                        =                        fun3(x)

 f3  =  (pp(j)-ppi(j))*rp  -  (2*c1*c2*((rs(j)/rrs)*x)^2)/(1-c2*(((rs(j)/rrs)*x)^4-1))  -  2*c3;

end
```

```
function out1 = odefun1(t,y,yp)

delta = (rrs.*cos(t)).^2+(ss.*sin(t)).^2;
ls = rs(j).*yp./sqrt(delta);
lt = rs(j).*sin(y)./(rrs.*sin(t));
q = c2*((ls*lt)^2-1);
out1 = (pp(j)-ppo(j))*rs(j) - 2*c1*ls*lt*c2/(1-q) - 2*c3;

end
```

```
function out3 = odefun3(t,y,yp)

delta = (rrs.*cos(t)).^2+(ss.*sin(t)).^2;
ls = rp.*yp./sqrt(delta);
lt = rp.*sin(y)./(rrs.*sin(t));
q = c2*((ls*lt)^2-1);
out3 = (pp(j)-ppi(j))*rp  - 2*c1*ls*lt*c2/(1-q) - 2*c3;
end

end
```

Material Deformation Optimisation MatLab Code (simP.m)

This code uses the same logic as the cteIdnt.m to optimize a set of *Lp* for the materiel constants c1 c2 c3. It will not be further detailed, refer to cteIdnt.m for information and logic flow.

```
clc
clear
format long

global rp rrs ss C ppi ppo v0

shaperatio = 0.32;   % shaperatio
rp = 0.45E-6; % Pipette radius (m)
v0 = 6.05E-18; % Volume of intact platelet (m^3)
C = [5.435 2.832e-4 -1.302e-3]; % Materiel constants c1 c2 c3
deltap = [1; 2; 3; 4; 5; 6]; % Aspiration pressure (cmH20)
deltap = deltap.*98.067; % Aspiration pressure (Pa)


ppo = 101300.*ones(length(deltap),1);
ppi = ppo - deltap;
rrs = (3*v0/(4*pi*shaperatio))^(1/3);
ss = shaperatio*rrs;
C = [5.435 2.832e-4 -1.302e-3];


% options for Levenberg-Marquardt method of solution
options=optimset('MaxFunEvals',1e100,'tolFun',1e-3,'TolX',1e-
3,'MaxIter',5e3,'Algorithm','levenberg-marquardt');
warning off all;

lb = 1.1*ones(length(deltap),1).*rp;

inilp = [1e-6 1.5e-6  2e-6 2.5e-6 3e-6 4e-6]; % initial guesses for aspiration length

lp = lsqnonlin(@errLlp,inilp,lb,[],options); % the optimizer calls the @errLlp m-file

figure
plot(deltap.*rp, lp./rp,'.')
xlabel('P*Rp (N/m)')
ylabel('Lp/Rp (-)')
```

Material Deformation Optimisation MatLab Code (errLlp.m)

```
function error=errLlp(lp)

% Declare global variables
global rp rrs ss C ppi ppo v0

c1 = C(1);
c2 = C(2);
c3 = C(3);

rs=zeros(length(lp),1);
for i=1:length(lp)
 f = @(x) v0 - pi*(4/3*x^3 - 1/3*(x - sqrt(x^2 - rp^2))^2*(2*x + sqrt(x^2 - rp^2)) + 2/3*rp^3
+ (lp(i) - rp)*rp^2);
 options = optimset('TolX',1e-20,'TolFun',1e-32, 'Display', 'off');
 rs(i) = fzero(f,rrs,options); % finds rs such that platelet volume is preserved during
aspiration
end
pp = (ppo.*rs-ppi.*rp)./(rs-rp);

resolution = 100;
eps = 1e-8;
options1 = optimset('TolX',1e-12,'TolFun',1e-20, 'Display', 'off');
options2 = odeset('RelTol',1e-6,'AbsTol',1e-6);

% Zone 1 : external sphere

yp01 = zeros(length(lp),1);
t1s = zeros(length(lp),1);
for j = 1:length(lp)
 yp01(j) = fsolve(@fun1,2,options1);
end
t01 = pi-eps;
y01 = pi-yp01.*eps;
tspan1 = [t01,0];
for j = 1:length(lp)
 sol1 = ode15i(@odefun1,tspan1,y01(j),yp01(j),options2);
 t1 = linspace(min(sol1.x),max(sol1.x),resolution);
 y1 = deval(sol1,t1,1);
 y1s = asin(rp/rs(j));
 t1s(j) = interp1(y1,t1,y1s);
end

% Zone 3 : internal hemisphere

yp03 = zeros(length(lp),1);
t3t = t1s;
for j = 1:length(lp)
 yp03(j) = fsolve(@fun3,1,options1);
```

```
end
y03 = yp03.*eps;
tspan3 = [eps,pi];
for j = 1:length(lp)
 sol3 = ode15i(@odefun3,tspan3,y03(j),yp03(j),options2);
 t3 = linspace(min(sol3.x),max(sol3.x),resolution);
 y3 = deval(sol3,t3,1);
 y3t = pi/2;
 t3t(j) = interp1(y3,t3,y3t);
end

% Zone 2 : cylinder

error = zeros(length(lp),1);
for j = 1:length(lp)
 t2 = linspace(t3t(j),t1s(j),resolution);
 ls2 = ones(1,resolution);
  for i =1:resolution
    lt2 = rp/(rrs*sin(t2(i)));
    ls2(i) = fsolve(@fun2,1,options1);
 end
 int2 = trapz(t2,ls2.*sqrt((rrs.*cos(t2)).^2+(ss.*sin(t2)).^2));
 error(j) = (lp(j)-rp-int2)./(lp(j)-rp);
end

function f1 = fun1(x)

f1 = (pp(j)-ppo(j))*rs(j) - (2*c1*c2*((rs(j)/rrs)*x)^2)/(1-c2*(((rs(j)/rrs)*x)^4-1)) - 2*c3;

end

function f2 = fun2(x)

f2 = (pp(j)-ppi(j))*rp - (2*c1*c2*((rs(j)/rrs)*x)^2)/(1-c2*(((rs(j)/rrs)*x)^4-1)) - 2*c3;

end

function f3 = fun3(x)

 f3 = (pp(j)-ppi(j))*rp - (2*c1*c2*((rs(j)/rrs)*x)^2)/(1-c2*(((rs(j)/rrs)*x)^4-1)) - 2*c3;
end

function out1 = odefun1(t,y,yp)

delta = (rrs.*cos(t)).^2+(ss.*sin(t)).^2;
ls = rs(j).*yp./sqrt(delta);
lt = rs(j).*sin(y)./(rrs.*sin(t));
q = c2*((ls*lt)^2-1);
out1 = (pp(j)-ppo(j))*rs(j) - 2*c1*ls*lt*c2/(1-q) - 2*c3;

end

function out3 = odefun3(t,y,yp)
```

```
delta = (rrs.*cos(t)).^2+(ss.*sin(t)).^2;
ls = rp.*yp./sqrt(delta);
lt = rp.*sin(y)./(rrs.*sin(t));
q = c2*((ls*lt)^2-1);
out3 = (pp(j)-ppi(j))*rp  - 2*c1*ls*lt*c2/(1-q) - 2*c3;
end

end
```

Plot of Mechanical Reponses (ctePlot.m)

This code again uses the same logic as the previous 2 codes, with the exception it goes into more details when comes time to assess $\frac{d\varphi}{d\Phi}$ values for each Φ. This allows to compute tension as each Φ points.

```
clc
clear
format long

global pp ppo ppi rs rrs ss rp v0 c1 c2 c3 i lt2

shaperatio = 0.32;
c1 = 5.435;
c2 = 2.83e-4;
c3 = -1.3e-3;
rp = 0.45e-6;
v0 = 6.05e-18;
eps = 1e-8;
resolution = 100;
ppo = 101300;
rrs = (3*v0/(4*pi*shaperatio))^(1/3);
ss = shaperatio*rrs;
options1 = optimset('TolX',1e-12,'TolFun',1e-20, 'Display', 'off');
options2 = odeset('RelTol',1e-6,'AbsTol',1e-6);
warning off all;


for j = 1:1:4
    deltap =(j-1)*1+1;        % aspiration pressure (cm H20)
    deltap = deltap*98.067;   % aspiration pressure (Pa)
    ppi = ppo - deltap;

    lp = (16490*(deltap*rp)+2.2049)*rp;

    f = @(x) v0 - pi.*(4./3.*x.^3 - 1./3.*(x - sqrt(x.^2 - rp.^2)).^2.*(2.*x + sqrt(x.^2 -
rp.^2)) + 2./3.*rp.^3 + (lp - rp).*rp.^2);
    options = optimset('TolX',1e-20,'TolFun',1e-32, 'Display', 'off');
    rs = fzero(f,rrs,options); %Finds rs such that volume is constant.

    pp = (ppo.*rs-ppi.*rp)./(rs-rp);

    % Zone 1 : external sphere

    yp01 = fsolve(@fun1,2,options1);
    t01 = pi-eps;
    y01 = pi-yp01.*eps;
    tspan1 = [t01,0];
```

```
    sol1 = ode15i(@odefun1,tspan1,y01,yp01,options2); % find dphi/dPHI

    t1 = linspace(min(sol1.x),max(sol1.x),resolution);
    y1 = deval(sol1,t1,1);
    y1s = asin(rp./rs);
    t1s = interp1(y1,t1,y1s);% find PHI1

    t1 = linspace(t1s,max(sol1.x),resolution);
    [y1, dy1] = deval(sol1,t1,1); % find values of phi and dphi between PHI1 and numerical
boundary PHI=0
    ls1 = rs.*dy1./(sqrt((rrs.*cos(t1)).^2+(ss.*sin(t1)).^2)); % Eval meridional stretch
ratio.
    lt1 = rs.*sin(y1)./(rrs.*sin(t1)); % Eval equatorial stretch ratio
    q = c2.*((ls1.*lt1).^2-1);
    tension1 = c1*ls1.*lt1.*c2./(1-q) + c3; % Eval isometric tension from stretch ratios.

    % Zone 3 : internal hemisphere

    yp03 = fsolve(@fun3,1,options1);
    y03 = yp03.*eps;
    tspan3 = [eps,pi];
    sol3 = ode15i(@odefun3,tspan3,y03,yp03,options2);
    t3 = linspace(min(sol3.x),max(sol3.x),resolution);
    y3 = deval(sol3,t3,1);
    y3t = pi/2;
    t3t = interp1(y3,t3,y3t);
    t3 = linspace(min(sol3.x),t3t,resolution);
    [y3, dy3] = deval(sol3,t3,1);
    ls3 = rp.*dy3./(sqrt((rrs.*cos(t3)).^2+(ss.*sin(t3)).^2));
    int3 = trapz(t3,ls3.*sqrt((rrs.*cos(t3)).^2+(ss.*sin(t3)).^2));
    ref3 = rp.*y3t;
    err3 = (ref3-int3).*100./ref3;
    lt3 = rp.*sin(y3)./(rrs.*sin(t3));
    q = c2.*((ls3.*lt3).^2-1);
    tension3 = c1*ls3.*lt3.*c2./(1-q) + c3;

    % Zone 2 : cylinder

    t2 = linspace(t3t,t1s,resolution);
    lt2 = rp./(rrs.*sin(t2));
    for i =1:resolution
        ls2(i) = fsolve(@fun2,1,options1);
    end
    int2 = trapz(t2,ls2.*sqrt((rrs.*cos(t2)).^2+(ss.*sin(t2)).^2));
    ref2 = lp-rp;
    err2 = (ref2-int2).*100./ref2;
    q = c2.*((ls2.*lt2).^2-1);
    tension2 = c1*ls2.*lt2.*c2./(1-q) + c3;

    for i = 1:resolution
        y2(i) = pi/2;
    end
```

```
    t = [t1,t2,t3];         % PHI in theory
    y = [y1,y2,y3];         % phi in theory

    rr1 = rs.*sin(y1);
    zz1 = rs.*(1+cos(y1));
    rr3 = rp.*sin(y3);
    zz3 = rs.*(1+cos(y1s))+lp-rp.*(1-cos(y3));
    for i = 1:resolution
         rr2(i) = rp;
         zz2(i) = rs.*(1+cos(y1s))+(1-(i-1)./(resolution-1))*(lp-rp);
    end

    tt = linspace(0,pi,resolution);
    rr0 = rrs.*sin(tt).*10^6;     % Capital r in theory
    rr0s = rrs.*sin(t1s).*10^6;
    rr0t = rrs.*sin(t3t).*10^6;
    zz0 = ss.*(1+cos(tt)).*10^6;  % Capital z in theory
    zz0s = ss.*(1+cos(t1s)).*10^6;
    zz0t = ss.*(1+cos(t3t)).*10^6;
    current_rr0s = rr2(resolution).*10^6;
    current_zz0s = zz2(resolution).*10^6;
    current_rr0t = rr2(1).*10^6;
    current_zz0t = zz2(1).*10^6;

    subplot(1,3,1);
    plot(rr0,zz0,'k-','LineWidth',3)
    axis ([0 7.2*5/19.9 0 5])
    xlabel('r (microns)')
    ylabel('z (microns)')
    hold on
    plot(rr1.*10^6,zz1.*10^6,'r:','LineWidth',2)
    hold on
    plot(rr2.*10^6,zz2.*10^6,'r:','LineWidth',2)
    hold on
    plot(rr3.*10^6,zz3.*10^6,'r:','LineWidth',2)
    hold on

plot(rr0s,zz0s,'ks',rr0t,zz0t,'ko',current_rr0s,current_zz0s,'ks',current_rr0t,current_zz0t,'
ko','MarkerSize',8)
    hold on

    subplot(1,3,2);
    plot(ls1,zz1.*10^6,'g-',lt1,zz1.*10^6,'b-','LineWidth',2);
    xlabel('Circumferential (blue) and meridional (green) stretch ratios (-)')
    axis ([0 2.5 0 5])
    hold on
    plot(ls2,zz2.*10^6,'g-',lt2,zz2.*10^6,'b-','LineWidth',2);
    hold on
    plot(ls3,zz3.*10^6,'g-',lt3,zz3.*10^6,'b-','LineWidth',2);
    hold on

    subplot(1,3,3);
    plot(tension1.*10^4,zz1.*10^6,'r-','LineWidth',2);
```

```
    axis ([0 1.4 0 5])
    xlabel('Isotropic membrane tension (x 10^-^4 N/m)')
    hold on
    plot(tension2.*10^4,zz2.*10^6,'r-','LineWidth',2);
    hold on
    plot(tension3.*10^4,zz3.*10^6,'r-','LineWidth',2);
    hold on

end
```

Appendix B: Copyrighted Contents

ELSEVIER LICENSE
TERMS AND CONDITIONS

Apr 05, 2015

This is a License Agreement between Mathieu Sayeur ("You") and Elsevier ("Elsevier") provided by Copyright Clearance Center ("CCC"). The license consists of your order details, the terms and conditions provided by Elsevier, and the payment terms and conditions.

All payments must be made in full to CCC. For payment instructions, please see information listed at the bottom of this form.

Supplier	Elsevier Limited The Boulevard,Langford Lane Kidlington,Oxford,OX5 1GB,UK
Registered Company Number	1982084
Customer name	Mathieu Sayeur
Customer address	449 Boul Saint-Raymond Gatineau, QC J9A 1X3
License number	3602631218869
License date	Apr 05, 2015
Licensed content publisher	Elsevier
Licensed content publication	Elsevier Books
Licensed content title	Platelets
Licensed content author	Anthony A. Bavry
Licensed content date	2013
Number of pages	28
Start Page	117
End Page	144
Type of Use	reuse in a thesis/dissertation
Portion	figures/tables/illustrations
Number of figures/tables /illustrations	4
Format	print
Are you the author of this Elsevier chapter?	No
Will you be translating?	No
Original figure numbers	Figures 7-1, 7-3, 7-24, 7-34
Title of your thesis/dissertation	Mechanical Modeling of Human Platelets Membrane

7 Bibliography

Agnihotri, A., Soman, P., & Siedlecki, C. A. (2009). AFM measurements of interactions between the platelet integrin receptor GPIIbIIIa and fibrinogen. *Colloids and Surfaces B: Biointerfaces, 71*(1), 138-147. doi:10.1016/j.colsurfb.2009.01.019

Arya, M., Anvari, B., Romo, G. M., Cruz, M. A., Dong, J., McIntire, L. V., . . . Lopez, J. (2002). Ultralarge multimers of von willebrand factor form spontaneous high-strength bonds with the platelet glycoprotein ib-IX complex: Studies using optical tweezers. *Blood, 99*(11), 3971-3977.

Arya, M., López, J. A., Romo, G. M., Dong, J., McIntire, L. V., Moake, J. L., & Anvari, B. (2002). Measurement of the binding forces between von willebrand factor and variants of platelet glycoprotein ibα using optical tweezers. *Lasers in Surgery and Medicine, 30*(4), 306-312. doi:10.1002/lsm.10044

Buller, H. R. (2009). In Oudkerk M., Beek E. J. R. v. and Büller H. R. (Eds.), *Deep vein thrombosis and pulmonary embolism*. Chichester, UK ; Hoboken, NJ; Chichester, West Sussex ; Hoboken, NJ:

Burns, G., & Dodge, J. (1984). Theophylline inhibits platelet aggregation, prostaglandin and thromboxane production by a mechanism which is independent of cyclic AMP. *Agents and Actions, 14*(1), 102-108. doi:10.1007/BF01966841

Canadian Blood Services. (2014). Circular of information, platelets, leukocyte reduced (LR). RetrievedMarch/22,2015,from https://www.blood.ca/sites/default/files/PooledApheresisPlatelets.pdf

Dobesh, P. P. (2009). Economic burden of venous thromboembolism in hospitalized patients. *Pharmacotherapy, 29*(8), 943. doi:10.1592/phco.29.8.943

Edmunds, L. H., Mckinlay, S., Anderson, J. M., Callahan, T. H., Chesebro, J. H., Geiser, E. A., . . . Didisheim, P. (1997). Directions for improvement of substitute heart valves: National heart, lung, and blood institute's working group report on heart valves. *Journal of Biomedical Materials Research, 38*(3), 263.

Ethier, C. R., & Ethier, C. R., 1959-. (2007). In Simmons C. A., Ethier C. R. and Simmons C. A. (Eds.), *Introductory biomechanics : From cells to organisms*. Leiden; Cambridge ; New York: Leiden Cambridge University Press.

Evans, E., & Yeung, A. (1989a). Apparent viscosity and cortical tension of blood granulocytes determined by micropipet aspiration. *Biophysical Journal, 56*(1), 151-160. doi:10.1016/S0006-3495(89)82660-8

Evans, E., & Yeung, A. (1989b). Apparent viscosity and cortical tension of blood granulocytes determined by micropipet aspiration. *Biophysical Journal, 56*(1), 151-160. doi:10.1016/S0006-3495(89)82660-8

Evans, E. A. (1973). A new material concept for the red cell membrane. *Biophysical Journal, 13*(9), 926-940. doi:10.1016/S0006-3495(73)86035-7

Flaumenhaft, R. (2013). Chapter 18 - platelet secretion. In A. D. Michelson (Ed.), *Platelets (thirdedition)*(pp.343-366)AcademicPress. doi:http://dx.doi.org.proxy.bib.uottawa.ca/10.1016/B978-0-12-387837-3.00018-3

Frojmovic, M. M., & Panjwani, R. (1976). Geometry of normal mammalian platelets by quantitative microscopic studies. *Biophysical Journal, 16*(9), 1071-1089. doi:10.1016/S0006-3495(76)85756-6

Fung, Y. C. B., & Tong, P. (1968). Theory of the sphering of red blood cells. *Biophysical Journal, 8*(2), 175-198. doi:10.1016/S0006-3495(68)86484-7

Gaczynska, M., & Osmulski, P. A. (2008). AFM of biological complexes: What can we learn? *Current Opinion in Colloid & Interface Science, 13*(5), 351-367. doi:10.1016/j.cocis.2008.01.004

Gibbins, J. M., & Mahaut-Smith, M. (2004). *Platelets and megakaryocytes*. Totowa, N.J.: Totowa, N.J. : Humana Press, c2004.

Golan, D. E., & Tashjian, A. H. (2012). *Principles of pharmacology the pathophysiologic basis of drug therapy* (3rd ed.. ed.). Philadelphia: Philadelphia : Wolters Kluwer Health/Lippincott Williams & Wilkins, c2012.

Gulcan, M., Varol, E., Etli, M., Aksoy, F., & Kayan, M. (2012). Mean platelet volume is increased in patients with deep vein thrombosis. *Clinical and Applied Thrombosis-Hemostasis, 18*(4), 427-430. doi:10.1177/1076029611427437

Guo, H., & Li, Z. (2013). Optical tweezers technique and its applications. *Science China Physics, Mechanics and Astronomy, 56*(12), 2351-2360. doi:10.1007/s11433-013-5355-3

Haga, J., Beaudoin, A., White, J., & Strony, J. (1998). Quantification of the passive mechanical properties of the resting platelet. *Annals of Biomedical Engineering, 26*(2), 268-277. doi:10.1114/1.118

Hartwig, J. H. (2013). Chapter 8 - the platelet cytoskeleton. In A. D. Michelson (Ed.), *Platelets (third edition)* (pp. 145-168) Academic Press. doi:http://dx.doi.org.proxy.bib.uottawa.ca/10.1016/B978-0-12-387837-3.00008-0

Haslam, R. J., & Lynham, J. A. (1972). Activation and inhibition of blood platelet adenylate cyclase by adenosine or by 2-chloroadenosine. *Life Sciences, 11*(23), 1143-1154. doi:10.1016/0024-3205(72)90269-X

Hayward, C. P. M., & Moffat, K. A. (2013). Chapter 28 - platelet aggregation. In A. D. Michelson (Ed.), *Platelets (third edition)* (pp. 559-580) Academic Press. doi:http://dx.doi.org.proxy.bib.uottawa.ca/10.1016/B978-0-12-387837-3.00028-6

Hochmuth, R. M. (2000). Micropipette aspiration of living cells. *Journal of Biomechanics, 33*(1), 15-22. doi:10.1016/S0021-9290(99)00175-X

Humphrey, J. D., 1959-. (2002). *Cardiovascular solid mechanics : Cells, tissues, and organs*. New York: New York : Springer, c2002.

Ji, B., & Bao, G. (2011). CELL AND MOLECULAR BIOMECHANICS: PERSPECTIVES AND CHALLENGES. *Acta Mechanica Solida Sinica; Acta Mech.Solida Sin., 24*(1), 27-51.

Karagkiozaki, V., Logothetidis, S., Kalfagiannis, N., Lousinian, S., & Giannoglou, G. (2009). Atomic force microscopy probing platelet activation behavior on titanium nitride nanocoatings for biomedical applications. *Nanomedicine: Nanotechnology, Biology, and Medicine, 5*(1), 64-72. doi:10.1016/j.nano.2008.07.005

Laufer, N., Grover, N. B., Ben-Sasson, S., & Freund, H. (1979). Effects of adenosine diphosphate, colchicine and temperature on size of human platelets. *Thrombosis and Haemostasis, 41*(3), 491-497.

Lee, I., & Marchant, R. E. (2000). Force measurements on platelet surfaces with high spatial resolution under physiological conditions. *Colloids and Surfaces B: Biointerfaces, 19*(4), 357-365. doi:10.1016/S0927-7765(00)00144-2

Levin, J. (2013). Chapter 1 - the evolution of mammalian platelets. In A. D. Michelson (Ed.), *Platelets (third edition)* (pp. 3-25) Academic Press. doi:http://dx.doi.org.proxy.bib.uottawa.ca/10.1016/B978-0-12-387837-3.00001-8

Lim, C. T., Zhou, E. H., & Quek, S. T. (2006). Mechanical models for living cells—a review. *Journal of Biomechanics, 39*(2), 195-216. doi:10.1016/j.jbiomech.2004.12.008

Litvinov, R. I., Barsegov, V., Schissler, A. J., Fisher, A. R., Bennett, J. S., Weisel, J. W., & Shuman, H. (2011). Dissociation of bimolecular aIIbß3-fibrinogen complex under a

constant tensile force. *Biophysical Journal, 100*(1), 165-173. doi:10.1016/j.bpj.2010.11.019

Liu, F., Wu, D., & Chen, K. (2014). A zebrafish embryo behaves both as a " cortical shell – liquid core" structure and a homogeneous solid when experiencing mechanical forces.*20*(6), 1841-1847. doi:10.1017/S1431927614013269

McGrath, B. (2009). *A mechanobiological investigation of platelets.* M.A.Sc. thesis University of Ottawa*,* 2009.

McGrath, B., Mealing, G., & Labrosse, M. (2011). A mechanobiological investigation of platelets. *Biomechanics and Modeling in Mechanobiology, 10*(4), 473-484. doi:10.1007/s10237-010-0248-0

Michelson, A. D. (2006). *Platelets* (2.th ed.). San Diego: San Diego : Elsevier, 2006.

Moskalensky, A. E., Yurkin, M. A., Konokhova, A. I., Strokotov, D. I., Nekrasov, V. M., Chernyshev, A. V., . . . Maltsev, V. P. (2013). Accurate measurement of volume and shape of resting and activated blood platelets from light scattering. *Journal of Biomedical Optics, 18*(1), 017001-017001. doi:10.1117/1.JBO.18.1.017001

National Blood Clot Alliance.Blood clots in the united states. Retrieved 04/07, 2015, from http://www.stoptheclot.org/index/blood-clots-in-the-united-states.htm

Neuman, K. C., & Block, S. M. (2004). Optical trapping. *Review of Scientific Instruments, 75*(9) doi:10.1063/1.1785844

Phillips, D. R., Teng, W., Arfsten, A., Nannizzi-Alaimo, L., White, M. M., Longhurst, C., . . . Scarborough, R. M. (1997). Effect of Ca2+ on GP IIb-IIIa interactions with integrilin: Enhanced GP IIb-IIIa binding and inhibition of platelet aggregation by reductions in the concentration of ionized calcium in plasma anticoagulated with citrate. *Circulation, 96*(5), 1488.

Radmacher, M., Fritz, M., Kacher, C. M., Cleveland, J. P., & Hansma, P. K. (1996). Measuring the viscoelastic properties of human platelets with the atomic force microscope. *Biophysical Journal, 70*(1), 556-567.

Skalak, R., Tozeren, A., Zarda, R. P., & Chien, S. (1973). Strain energy function of red blood cell membranes. *Biophysical Journal, 13*(3), 245-264. doi:10.1016/S0006-3495(73)85983-1

Song, Y., & Bhushan, B. (2008). Atomic force microscopy dynamic modes: Modeling and applications. *Journal of Physics: Condensed Matter, 20*(22), 225012. doi:10.1088/0953-8984/20/22/225012

Spyropoulos, A. C., & Lin, J. (2007). Direct medical costs of venous thromboembolism and subsequent hospital readmission rates: An administrative claims analysis from 30 managed care organizations. *Journal of Managed Care Pharmacy : JMCP, 13*(6), 475.

Sutter Instrument. (2015). Pipette cookbook 2015A. Retrieved Mars/22, 2015, from www.sutter.com/PDFs/pipette_cookbook.pdf

Van Vliet, K. J., Suresh, G., Van Vliet, S., & Bao, S. (2003). The biomechanics toolbox: Experimental approaches for living cells and biomolecules. *Acta Materialia, 51*(19), 5881-5905. doi:10.1016/j.actamat.2003.09.001

Wei Yin, W. Y., Bluestein, D., Jestyz, J., & Perrotta, P. (2002). *Flow induced platelet activation in mechanical heart valves - in vitro studies* doi:10.1109/IEMBS.2002.1106557

White, J. G. (2013). Chapter 7 - platelet structure. In A. D. Michelson (Ed.), *Platelets (third edition)* (pp. 117-144) Academic Press. doi:http://dx.doi.org.proxy.bib.uottawa.ca/10.1016/B978-0-12-387837-3.00007-9

White, J. G., Burris, S. M., Tukey, D., Smith 2nd, C., & Clawson, C. C. (1984). Micropipette aspiration of human platelets: Influence of microtubules and actin filaments on deformability. *Blood, 64*(1), 210-214.

White, R. H. (2003). The epidemiology of venous thromboembolism. *Circulation, 107*(23), I4.

Williams, M. C. (2002). Optical tweezers: Measuring piconewton forces. *Biophysics Textbook Online: Http://Www.Biophysics.Org/Btol,*

Yeung, A., & Evans, E. (1989). Cortical shell-liquid core model for passive flow of liquid-like spherical cells into micropipets. *Biophysical Journal, 56*(1), 139-149. doi:10.1016/S0006-3495(89)82659-1